Earth Syst. Sci. Data, 10, 355–390, 2018
https://doi.org/10.5194/essd-10-355-2018

Open Access Earth System Science Data

A 20-year record (1998–2017) of permafrost, active layer and meteorological conditions at a high Arctic permafrost research site (Bayelva, Spitsbergen)

Julia Boike[1,2], Inge Juszak[1], Stephan Lange[1], Sarah Chadburn[3,4], Eleanor Burke[5], Pier Paul Overduin[1], Kurt Roth[6], Olaf Ippisch[7], Niko Bornemann[1], Lielle Stern[6], Isabelle Gouttevin[8,9], Ernst Hauber[10], and Sebastian Westermann[11]

[1]Alfred Wegener Institute Helmholtz Center for Polar and Marine Research, Telegrafenberg A43, 14473 Potsdam, Germany
[2]Humboldt University, Geography Department, Unter den Linden 6, 10099 Berlin, Germany
[3]University of Leeds, School of Earth and Environment, Leeds, LS2 9JT, UK
[4]University of Exeter, College of Engineering, Mathematics and Physical sciences, Exeter, EX4 4QF, UK
[5]Met Office Hadley Centre, FitzRoy Road, Exeter, EX1 3PB, UK
[6]University of Heidelberg, Institute of Environmental Physics, INF 229, 69120 Heidelberg, Germany
[7]TU Clausthal, Institute for Mathematics, Erzstr. 1, 38678 Clausthal-Zellerfeld, Germany
[8]Irstea, UR HHLY, Centre de Lyon-Villeurbanne, 5 rue de la Doua, BP 32108, 69616 Villeurbanne CEDEX, France
[9]Université Grenoble Alpes, Irstea, UR ETGR, Centre de Grenoble, 2 rue de la Papeterie-BP 76, 38402 St-Martin-d'Hères, France
[10]German Aerospace Center (DLR), Institute of Planetary Research, Rutherfordstr. 2, 12489 Berlin, Germany
[11]University of Oslo, Department of Geosciences, P.O. Box 1047, Blindern, 0316 Oslo, Norway

Correspondence: Julia Boike (Julia.Boike@awi.de)

Received: 5 September 2017 – Discussion started: 12 September 2017
Revised: 11 January 2018 – Accepted: 12 January 2018 – Published: 5 March 2018

Abstract. Most permafrost is located in the Arctic, where frozen organic carbon makes it an important component of the global climate system. Despite the fact that the Arctic climate changes more rapidly than the rest of the globe, observational data density in the region is low. Permafrost thaw and carbon release to the atmosphere are a positive feedback mechanism that can exacerbate global warming. This positive feedback functions via changing land–atmosphere energy and mass exchanges. There is thus a great need to understand links between the energy balance, which can vary rapidly over hourly to annual timescales, and permafrost, which changes slowly over long time periods. This understanding thus mandates long-term observational data sets.

Such a data set is available from the Bayelva site at Ny-Ålesund, Svalbard, where meteorology, energy balance components and subsurface observations have been made for the last 20 years. Additional data include a high-resolution digital elevation model (DEM) that can be used together with the snow physical information for snowpack modeling and a panchromatic image. This paper presents the data set produced so far, explains instrumentation, calibration, processing and data quality control, as well as the sources for various resulting data sets. The resulting data set is unique in the Arctic and serves as a baseline for future studies. The mean permafrost temperature is −2.8 °C, with a zero-amplitude depth at 5.5 m (2009–2017). Since the data provide observations of temporally variable parameters that mitigate energy fluxes between permafrost and atmosphere, such as snow depth and soil moisture content, they are suitable for use in integrating, calibrating and testing permafrost as a component in earth system models.

Published by Copernicus Publications.

The presented data are available in the Supplement for this paper (time series) and through the PANGAEA and Zenodo data portals: time series (https://doi.org/10.1594/PANGAEA.880120, https://zenodo.org/record/1139714) and HRSC-AX data products (https://doi.org/10.1594/PANGAEA.884730, https://zenodo.org/record/1145373).

1 Introduction

Permafrost, which is defined as ground that has remained frozen continuously for 2 years or more, covers large parts of the land surface in the Northern Hemisphere, amounting to about 15 million km^2 (Brown et al., 1998). The range in temperatures and water and ice content of the upper surface layer of seasonally freezing and thawing ground (the active layer) determines the biological and hydrological processes that operate in these areas. Thermal degradation of permafrost over the last few decades has been reported from 10 available circum-Arctic boreholes (Romanovsky et al., 2010) with a recent update by Romanovsky et al. (2017). Warming and thawing of permafrost and an overall reduction in the area that it covers under future climate change scenarios have been predicted in all recent climate models, but at widely varying rates (Koven et al., 2012). Continued observations, not only of permafrost thermal data but also of the multiple other types of data required to understand the changes to permafrost, are therefore of great importance. The data required include information on the upper boundary condition of the soil (specifically on snow cover), on atmospheric conditions and on various subsurface state variables (e.g., volumetric liquid water content). The seasonal snow cover in Arctic permafrost regions insulates the permafrost surface for many months of the year and has an important effect on the thermal regime of permafrost (Langer et al., 2013; López-Moreno et al., 2016). The soil's water content determines not only its hydrologic and thermal properties, but also the amount of latent heat that is either required for the seasonal thaw in spring or produced during fall. In view of these dependencies, the data sets (including snow cover and the thermal state of the soil and permafrost), ideally at the same resolution as any meteorological input data, will be of great value for evaluating permafrost models (or land surface models intended for permafrost regions). In this paper we present data that incorporate subsurface components of heat and mass flux, properties of the snow cover and weather data from the Bayelva high Arctic permafrost site.

The Bayelva research site on the Spitsbergen island in the Svalbard archipelago (78.551° N, 11.571° E) has been used for research by the Alfred Wegener Institute (AWI) in collaboration with academic partners since 1998, with the original objective of developing and testing permafrost process models (Ippisch, 2001; Stern, 2017). Major developments in earth system models, e.g., through the European PAGE21 project (http://www.page21.org), Permafrost Carbon Network projects (http://www.permafrostcarbon.org), and satellite calibration and validation missions, have subsequently led to sustained interest in the data produced from a wider modeling community. This publication provides information on the site and a full documentation of the data set collected between 1998 and 2017 that may be required for input into earth system models (Chadburn et al., 2017; Ekici et al., 2014, 2015).

2 Site description

The Bayelva site is located in the European high Arctic, on western Spitsbergen in the Svalbard archipelago. It is situated about 3 km from the small village of Ny-Ålesund, which serves as a permanent hub for researchers and their logistical support. Ny-Ålesund was a coal mining area from 1916 to 1962, since then the village has been gradually transformed into a research community. Long-term meteorological monitoring was initiated in 1969 by the Norwegian Sverdrup Station but research topics now also include terrestrial ecosystems, glacier monitoring, detailed atmospheric research and the Kongsfjorden ocean system, coordinated by the Ny-Ålesund Science Managers Committee (http://nysmac.npolar.no/).

The West Spitsbergen Current, a branch of the North Atlantic, warms this area to an average air temperature of between −17.0 and −3.8 °C in January and from 4.6 to 6.9 °C in July (18-year period: 1 August 1993 to 31 July 2011; Maturilli et al., 2013). It also provides about 400 mm of precipitation annually, which falls mostly as snow between September and May. Significant air temperature rise has been detected since 1960, which has generally been attributed to changes in the radiation budget and atmospheric circulation patterns (Førland et al., 2011; Hanssen-Bauer and Førland, 1998). This rise is also reflected in the permafrost temperatures, as recorded from deep boreholes in the mountains at Janssonhaugen (Isaksen et al., 2007a, b, 2001). For the 6-year period from 1999 to 2005 the borehole temperatures have increased: at 25 m by 0.26 °C, at 30 m by 0.19 °C and at 40 m by between 0.07 and 0.09 °C (Romanovsky et al., 2017). Continuous permafrost underlies the unglaciated coastal areas to a depth of about 100 m and the active layer thickness (ALT) at the end of summer ranges between 1 and 2 m (Humlum, 2005). ALT data are available from the Global Terrestrial Network for Permafrost (GTNP) database (http://gtnpdatabase.org/) for several locations on Svalbard but for different time periods and distances between 25 and

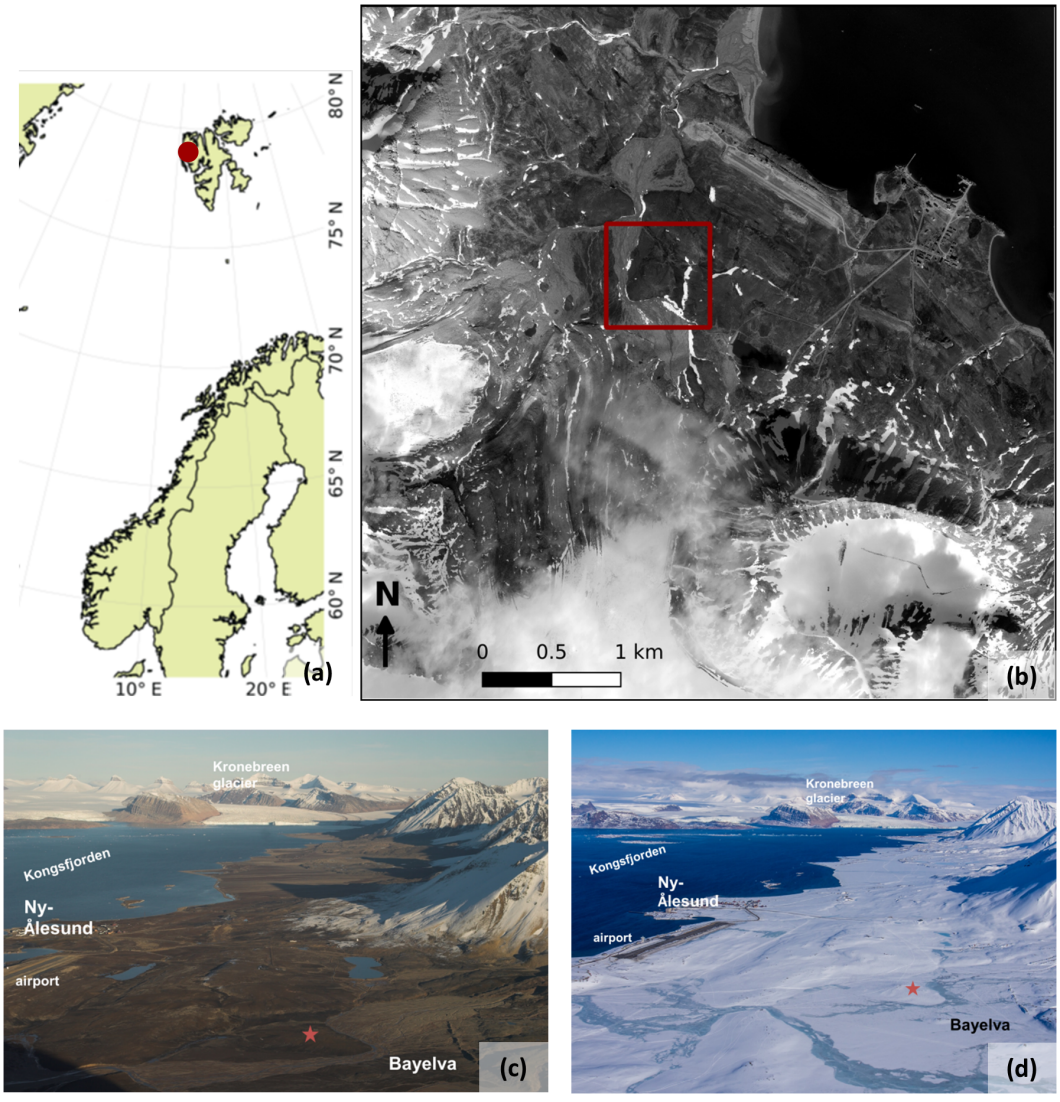

Figure 1. **(a)** Location of the Bayelva study site on Spitsbergen, western Svalbard, at 78.92094° N, 11.83334° E. **(b)** The site is located about 3 km from Ny-Ålesund in the Bayelva River catchment area, between two mountains (Zeppelinfjellet and Scheteligfjellet), and in front of the Brøggerbreen glacier. Aerial image captured in August 2008 using the high-resolution HRSC-AX camera (Hauber et al., 2011a, b): data and metadata for the high resolution the HRSC-AX image covering the entire area shown in **(b)** are provided in Appendix B. **(c)** The area of the site under summer conditions (August 2008) and **(d)** under spring conditions (April 2016).

115 km away from Bayelva. The site with the longest record, Janssonhaugen, is located 115 km to the southeast and had an average thaw depth of 175 cm for 1998–2013. The region has experienced increases in cloudiness, precipitation, and the number and intensity of cyclones in recent years, especially during the winter months (Hanssen-Bauer and Førland, 1998; Sepp and Jaagus, 2011). The increase in cloudiness (Maturilli and Kayser, 2016) has led to an increase in incoming long-wavelength radiation, resulting in a major change to the winter radiation budget for this region, as measured at the German–French (AWIPEV) research station, which is located within the village of Ny-Ålesund (Maturilli et al., 2014). This research station carries out long-term monitoring of radiation (Baseline Surface Radiation Network, BSRN; http://bsrn.awi.de/) and basic meteorological data (http://www.awipev.eu/). Additional meteorological data (e.g., air temperature at 10 m, wind speed and direction at 2 and 10 m) are available in Maturilli et al. (2013).

The data presented herein were collected from the high Arctic Bayelva River catchment area (Fig. 1), about 3 km away from Ny-Ålesund. A legacy from past mining activities is the physical disturbance of the ground in and around Ny-Ålesund (e.g., compaction and reworking of the soil). Traffic in the village (people, cars, snow mobiles) also affects the surface conditions, especially in winter. Thus, we chose a location that was sufficiently away to be unaffected by

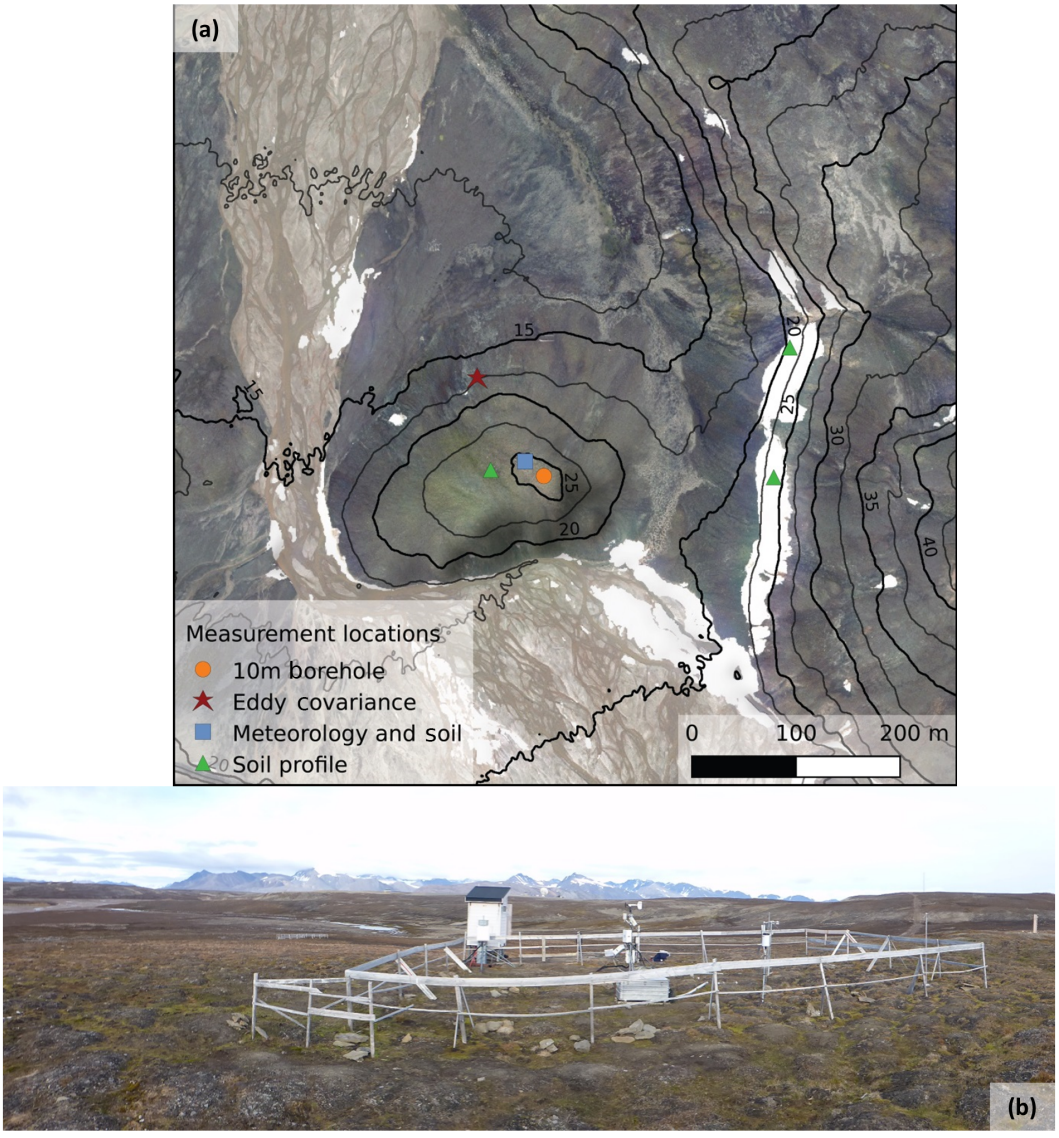

Figure 2. Topographical map **(a)** and overview of the Bayelva study site **(b)** in Ny-Ålesund, Svalbard. **(a)** Aerial orthoimage (20 cm px^{-1}) with topographic information (2.5 m contour lines) derived from a digital elevation model (DEM) with a cell size of 0.5 m. The locations of the instrumental and sampling sites are marked by colored symbols. The site is located on a small hill; white areas are snow fields remaining late in the season. The orthophoto and DEM were obtained with the HRSC-AX camera in August 2008 (data archived in Pangaea and metadata for the high-resolution DEM covering the entire area shown in Fig. 1b are provided in Appendix B). **(b)** Most of the instruments are within a fenced-off area to protect them from reindeer damage. Note that the eddy covariance station and permafrost borehole are located outside the fenced area.

these disturbances. The Bayelva catchment area lies between two mountains (Zeppelinfjellet and Scheteligfjellet), with the glacial Bayelva River originating from the two branches of the Brøggerbreen glacier. The terrain flattens out to the north of the Bayelva site and the Bayelva River flows into the Kongsfjorden fjord and the Arctic Ocean about 1 km from the site (Fig. 1). Over the past three decades the Bayelva catchment area has been the focus of intensive investigations into fluvial hydrology (sediment transfer and geochemistry; Hodson et al., 2002), soil and permafrost conditions (Boike et al., 2008b; Roth and Boike, 2001; Westermann, 2010; Westermann et al., 2011b), the surface energy balance (Boike et al., 2003b; Westermann et al., 2009), and the micrometeorological processes controlling the surface gas and energy exchanges (Lloyd, 2001b; Lloyd et al., 2001; Lüers et al., 2014). A permafrost maximum, minimum and average temperature with depth (trumpet curve) was shown for data for 1 year (August 2009–August 2010) by Boike et al. (2012). The data from this Bayelva site have also been used in earth system modeling (Ekici et al., 2014, 2015). Nearby investiga-

tions by Japanese and Italian researchers include vegetation analysis with respect to periglacial and glacial landforms and topography (Cannone et al., 2004; Ohtsuka et al., 2006), as well as investigations into the plant- and plot-scale dependence of CO_2 emissions on biotic and abiotic factors at the start and end of the growing season (Cannone et al., 2016; Uchida et al., 2006).

The Bayelva site is located on top of the Leirhaugen hill (25 m a.s.l.), on permafrost patterned ground (Fig. 2). The hill consists mainly of rock but is partly covered by a mixture of sediments that consist of glacial till, together with fine grained glaciofluvial sediments and clays from the last glacial advance, likely deposited by the Kongsfjorden glacier (J. Tolgensbakk, personal communication, 2007). According to the geological map, the site is part of the Brøggerbreen formation (lithography sandstone, shale, conglomerate), but the gray color of the sediments suggests that the material was deposited by the Kongsfjorden glacier and not the adjacent Brøggerbreen glacier, which deposits redder material. Thus, the site is part of the Kongsfjorden Formation, with the main lithography sandstone, shale and coal (Hjelle et al., 1999). Since the hill has a maximum altitude of about 38 m, which is below the upper marine limit, these sediments may also include marine deposits.

The vegetation cover in the vicinity of the Bayelva site (i.e., the area of the hill) has been estimated to be approximately 50–60 %, with the remainder being bare soil with a small proportion of stones (cobbles and gravel) (Lloyd et al., 2001). Within the rest of the Bayelva River catchment area, sparse vegetation alternates with bare soil and sand, or with rock fields.

The area of the Bayelva site is covered with non-sorted circles, also known as mudboils (Fig. 2), which are only present on the hill itself, with other patterned ground phenomena (such as sorted circles and stripes) occurring on and in the area surrounding Leirhaugen hill. These non-sorted circles formed under localized favorable conditions following the last glacial period. The bare soil centers of these circles are about 1 m in diameter, surrounded by a vegetated rim that consists of a mixture of low vascular plants (including various species of grass and sedge such as *Carex* spp., *Deschampsia* spp., *Eriophorum* spp., *Festuca* spp. and *Luzula* spp.), catchfly, saxifrage, willow, various other locally common species (*Dryas octopetala*, *Oxyria digyna*, *Polygonum viviparum*), and some unclassified species of moss and lichen (Ohtsuka et al., 2006; Uchida et al., 2006).

The soils on the hill generally range from silty loam to silty clay with a few large stones. The silt content decreases from more than 50 % at the top of the soil profile to less than 30 % at the bottom of the soil profile at about 1 m depth, while the clay content increases to more than 50 %. Concentrations of total organic carbon, total nitrogen and total sulphur are highest at the bottom of the soil profile, peaking below the centers of the non-sorted circles. The organic carbon concentration is high (> 6 % weight) at the bottom of the soil profile. Nitrogen is elevated beneath the vegetated rim of the non-sorted circles (Boike et al., 2008a).

The Bayelva site can be temporarily shaded from direct solar radiation by the mountains on either side. Snow is present for up to 9 months of the year and strong winds can encourage drifting and snow redistribution. The snow depth varies within the Bayelva catchment area, as do its physical characteristics, such as the snow water equivalent and the internal stratigraphy and density of the snowpack. A 15 m × 10 m fence surrounds the Bayelva site to prevent reindeer from damaging the equipment, and a small wooden container (about 0.90 m × 1.40 m, and 2.3 m high) houses the data acquisition and transfer system (Fig. 2). Warm weather events during the winter can interrupt the build-up of snow cover resulting in the formation of either internal ice lenses or basal ice, depending on the heat content of the snowpack. Table 1 summarizes the characteristics of the site retrieved from both previous publications and data included in this paper.

3 Data description

The Bayelva site was powered by a solar panel and wind generator during the period from 1998 to 2013 and data were retrieved manually through site visits every 4 to 6 weeks, when visual inspections were made of the sensors.

Since 2013 the site has been connected to the main electricity supply and the Ny-Ålesund data network, and data have since then been transferred automatically resulting in much improved data collection with almost no data gaps. The data gaps prior to 2013 resulted mainly from problems with the energy supply for the site, such as problems with the solar and wind charge regulator. The current online data transfer and real time data visualization enables real time data checking and identification of possible sensor failure, as well as remote programming. Major problems that have affected the continuous data collection or the data quality include reindeer disturbance (e.g., reindeer pulling cables out of the ground or destroying sensors by rubbing against the stations, as occurred in 2003) and the gradual uplift of sensors as a result of freeze–thaw processes, which affected soil temperature measurements.

Details of the sensors are provided in the following sections, as well as descriptions of the data quality and cleaning routine (Sect. 4). The instruments are divided into above-ground (meteorological) and below-ground sensors (e.g., soil sensors). Further detailed information on the sensors can be found in Table 2, which summarizes all of the parameters and instruments (Table 2), as well as in Appendices C and D (metadata and description of instruments). Figure 3 presents time series of parameters between 1998 and 2017.

Table 1. Site description parameter for earth system model input. Values have been computed and compiled for the Bayelva site and surrounding areas.

Variable	Value	Source
Surface characteristic		
Summer albedo	0.15	Westermann et al. (2009)
Summer Bowen ratio	1 (0.25–2)	Westermann et al. (2009)
Summer roughness length (mm)	1 (by fitting an energy balance model) 7 (eddy covariance)	Westermann (2010)
Snow properties		
Snow albedo	Average for snow-covered period prior to melt: 0.81 (2009–2016)	This paper
End of the snow ablation	8 June–11 July	This paper (1999–2016)
Maximum snow depth (end of season before ablation) (m)	Range: 0.65–1.42, average: 0.9	This paper (1999–2016)
End-of-season snow density ($kg\,m^{-3}$)	350 ± 50	Boike et al. (2003a); Westermann et al. (2009) Appendix E for individual profiles
Snow thermal conductivity ($W\,m^{-1}\,K^{-1}$)	0.34	Computed from snow density of $370\,kg\,m^{-3}$ using Yen (1981)
Snow thermal conductivity ($W\,m^{-1}\,K^{-1}$)	0.45 ± 0.15	Westermann et al. (2009)
Soil properties		
Organic layer thickness	0–5 cm (bare to vegetated areas; up to 15 cm in wetter areas)	This paper
Thawed soil thermal conductivity ($W\,m^{-1}\,K^{-1}$)	1.3 ± 0.4 at volumetric soil liquid water content 20–40 % (soil profile 1998: profile average)	Westermann et al. (2009)
Soil heat capacity thawed ($10^6\,J\,K^{-1}\,m^{-3}$)	2.3 ± 0.5 at volumetric liquid water content 20–40 %	Westermann et al. (2009)
Frozen soil thermal conductivity ($W\,m^{-1}\,K^{-1}$)	2.0–2.5	Westermann et al. (2011a) based on thermal diffusivity provided by Roth and Boike (2001)
Soil texture	Silty clay to sandy silt, stone content < 10 % at surface with up to 50 %	Boike et al. (2008a) Appendix F for individual pedons
Soil bulk density ($kg\,m^{-3}$)	Average: $1.9 \times 10^3\,kg\,m^{-3}$	Boike et al. (2008a) Roth and Boike (2001) Appendix F for individual pedons
Soil carbon density ($kg\,C\,m^{-3}$)	$6\,kg\,m^{-3}$ (down to 78 cm) 0–60 $kg\,m^{-3}$ (range) 2–22 $kg\,m^{-3}$ (range over averaged vertical profile)	Chadburn et al. (2017) Appendix F for individual pedons
Organic carbon stock ($kg\,C\,m^{-2}$)	4.3 (range: 1.1–7.9 $kg\,C\,m^{-2}$) (0–100 cm)	Area between flood plain and sea (Yoshitake et al., 2011). Appendix F for individual pedons
Saturated hydraulic conductivity ($m\,s^{-1}$)	10.9×10^{-6} 7.11×10^{-6}	Weismüller et al. (2011) Ekici et al. (2015)
Clapp–Hornberger exponent (b factor)	5 (for silty loam soil)	Beringer et al. (2001)
porosity (volumetric water content at saturation)	0.36–0.5	Roth and Boike (2001) Weismüller et al. (2011)
Van Genuchten parameters: alpha ($1\,mm^{-1}$)	Alpha = 0.002	Weismüller et al. (2011)
Van Genuchten parameters: n (unit-free)	1.2–1.5	Weismüller et al. (2011)

Table 1. Continued.

Variable	Value	Source
Vegetation characteristics		
Vegetation height	0–20 cm (bare soil to vegetated areas)	This paper
Vegetation fractional coverage	50–60 area %,	This paper
	vascular plants cover up to 30 %	Lloyd (2001a)
Vegetation type	"Lichen heath"	Brattbakk (1981)
	"High Arctic tundra in mesic–xeric conditions"	Cannone et al. (2004)
	"A mixed community of bryophytes (e.g., *Sanionia uncinata*, *Aulacomnium turgidum* and *Dicranoweisia* sp.) and vascular plants (e.g., *Salix polaris*, *Saxifraga oppositifolia*, *Oxyria digyna* and *Dryas octopetala*) covered the well-developed vegetation among topographical undulation."	Uchida et al. (2009)
Leaf area index (LAI)	0 (no vegetation areas), 0.3–0.7,	Cannone et al. (2016)
Root depth	∼ 19 cm	This paper
Leaf dry biomass	26–195 g m^{-2} for small patches of 100 % vegetation cover of three different species	Muraoka et al. (2008)
Landscape		
Landscape type	Glacial outwash flood plain	This paper
Bioclimate subzones	subzones A and B, characterized by barren ground and scattered vegetation. The vegetation mainly consists of non-vascular plants (40 % cover) and a few vascular plants (5 % cover). The average total phytomass in this subzone is lower than 3 t ha^{-1} and the net annual production is lower than 0.3 t ha^{-1}.	CAVM-Team (2005)

3.1 Weather station data

Meteorological data have been recorded at the AWIPEV research base in Ny-Ålesund since 1992, including radiation component data for the worldwide Baseline Surface Radiation Network. The AWIPEV meteorological data are described by Maturilli et al. (2013) and can be downloaded from PANGAEA (http://bsrn.awi.de/data/data-retrieval-via-pangaea/). Climate records covering a longer period of time are available from Svalbard since 1898, with the establishment of a permanent weather station in 1911 (Førland et al., 2011).

Since the Bayelva site is located close to the leading edge of the Brøggerbreen glacier, a different local micro-climate can be expected from Ny-Ålesund. A climate station was therefore installed in 1998, within the fenced area. The temporal resolution of the meteorological measurements was increased in October 2009 from 60 to 30 min.

3.1.1 Air temperature, relative humidity and snow temperature

Air temperature and relative humidity (hourly averages, since 2009 half-hourly averages) are measured at a height of 2 m above the ground surface using PT100 platinum resistance temperature sensors and Rotronic MP103A and Vaisala HMP45 capacity sensors, protected by unventilated shields. The heights of the shields are not adjusted during periods of snow cover accumulation or ablation. The uncertainty in the temperature measurements ranges between 0.03 and 0.5 °C, depending on the sensors used; the uncertainty in the relative humidity measurements ranges between 2 and 3 %. The PT100 temperature sensors were calibrated in ice-slush water for at least 12 h to determine the absolute accuracy at 0 °C. The precision of the temperature sensors was calculated from the variation in values recorded during the calibration period, at constant temperatures in ice-slush water, and can be found in Table 2.

The change of sensors for relative humidity in 2009 resulted in a 7 percentage points lower average relative humidity between 2009 and 2017 as compared to the period before, independent of the season.

PT100 temperatures sensors were installed at the weather station in 1998, close to the ground surface. When covered by snow these sensors record the snow temperature, while during the snow-free period they record (unshielded) air temperatures. The temperature cables were originally attached to a small (vertical) bamboo stick, with sensors sticking out

Table 2. List of sensors, parameters and instrument characteristics for the automated time series data from the Bayelva site, 1998–2017. Additional (not automated) data on snow cover and soil profiles can be found in Appendices E and F. Positive heights are above surface; negative heights are below surface.

Variable	Sensor	Period of operation		Height (m)	Unit	Measuring interval	Integration method	Spectral range	(Field) accuracy (±)
		from	to						
Meteorological sensors									
Air temperature	Rotronic MP103A	Apr 2000	Aug 2009	2	°C	20 s	avg.[1] 1 h		0.5 °C (at −40 to +60 °C)
Air temperature	Vaisala HMP45	Aug 2009	…	2	°C	60 s	avg. 30 min		0.2 °C (at 20 °C)
Air temperature	1× PT100	Aug 1999	Aug 2009	8/1999[2]: 2 4/2000: 1	°C	15 min	avg. 1 h		0.03 °C
Air temperature	1× PT100	Aug 2009	…	1	°C	60 s	avg. 30 min		0.03 °C
Relative humidity	Rotronic MP103A	Apr 2000	Aug 2009	2	%	20 s	avg. 1 h		3 % (at 20 °C)
Relative humidity	Vaisala HMP45	Aug 2009	…	2	%	60 s	avg. 30 min		2 % (at 20 °C, 0–90 % RH); 3 % (at 20 °C, 90–100 % RH)
Wind direction	R.M. Young anemometer 05103	Sep 1998	Aug 2009	3	deg		avg. 1 h		3°
Wind direction	R.M. Young anemometer 05103	Aug 2009	…	3	deg		avg. 30 min		3°
Wind speed	R.M. Young anemometer 05103	Sep 1998	Aug 2009	3	$m\,s^{-1}$		avg. 1 h		0.3 $m\,s^{-1}$
Wind speed	R.M. Young anemometer 05103	Aug 2009	…	3	$m\,s^{-1}$		avg. 30 min		0.3 $m\,s^{-1}$
Net radiation	CS[3] Q7	Sep 1998	Apr 2000	1.14	$W\,m^{-2}$	20 s	avg. 1 h	0.25–60 µm	6–10 %
Net radiation	Kipp & Zonen NR Lite	Apr 2000	May 2002	1.14	$W\,m^{-2}$	20 s	avg. 1 h	0–100 µm	3–20 %
Net radiation	CS Q7	May 2002	Sep 2003	1.14	$W\,m^{-2}$	20 s	avg. 1 h	0.25–60 µm	6–10 %
Net radiation	Kipp & Zonen NR-LITE	Sep 2003	Aug 2009	1.6	$W\,m^{-2}$	20 s	avg. 1 h	0–100 µm	3–20 %
Incoming short-wave radiation	Skye Pyranometer SP1110	Sep 1998	Aug 2009	2	$W\,m^{-2}$	20 s	avg. 1 h	350–1100 nm	5 % (typically < ±3 %)
Outgoing long-wave radiation	Kipp & Zonen Pyrgeometer CG1	May 2002	Aug 2009	5/2002: 2.0 9/2003: 1.6	$W\,m^{-2}$	20 s	avg. 1 h	4.5–42 µm (50 % points)	10 % for daily totals
Four components radiation	Hukseflux NR01	Aug 2009	…	1.56	$W\,m^{-2}$	60 s	avg. 30 min	305–2800 nm[4]; 4500–50 000 nm	10 % for daily sums
Precipitation	Young 52203 unheated tipping bucket rain gauge	Sep 1998	Jul 2010	1.68	mm		sum 1 h		2 % (up to 25 $mm\,h^{-1}$)
Precipitation	Young 52203 unheated tipping bucket rain gauge	Jul 2010	…	1.68	mm		sum 30 min		2 % (up to 25 $mm\,h^{-1}$)
Snow sensors									
Snow depth	CS SR50 ultrasound	Sep 1998	Aug 2009	9/1999: 2.00 7/2001: 1.60 9/2003: 1.45	m		single 12 h		2.5 cm
Snow depth	CS SR50 ultrasound	Aug 2009	…	1.45	m		single 30 min		2.5 cm
Snow depth at eddy covariance site	CS SR50 ultrasound	Mar 2007	…	2.4	m	3 min	avg. 1 h		2.5 cm
Snow depth	Jenoptik SHM30 laser distance	Aug 2013	…		m		single 0.5 h		5 mm
Air–snow temperature	3× PT100	Aug 1999	Aug 2009	8/1999: 0.20; 0.35; 0.48 9/2003: 0.01; 0.20; 0.48 9/2004: 0.01; 0.20; 0.35	°C	15 min	avg. 1 h		0.1 °C
Air–snow temperature	2× PT100	Aug 2009	…	0.04; 0.2	°C	60 s	avg. 30 min		0.1 °C
Snow dielectric number	TDR Tektronix 1502B, SDM50 multiplexer, 1× TDR triple-wire 0.5 m	Sep 1998	Dec 2009	0–0.5 (vertical)			single 1 h		
Snow dielectric number	TDR100, SDM50 multiplexer, 1× CS605 probe, triple-wire 0.3 m	Aug 2009	…	0–0.3 (vertical)			single 1 h		

a few centimeters from the stick (Appendix C, Fig. C5). Visual inspections during late spring (May 2016) revealed that melting occurred around the bamboo stick, leaving an air gap around the stick. The temperature sensors were nevertheless well away from the stick (in a horizontal direction) and remained embedded in the snow. The height of the sensors was changed on a number of occasions following damage by reindeer. Sensors were originally mounted at heights of 0.35 and 0.48 m to record snow temperatures, but these heights were changed during subsequent years (Table 2). Information concerning the changes in sensor height is included in the data description that accompanies the data (Appendix C, Fig. C5).

Table 2. Continued.

Variable	Sensor	Period of operation		Height (m)	Unit	Measuring interval	Integration method	Spectral range	(Field) accuracy (±)
		from	to						
Soil sensors									
Soil temperature (2-D), profile (a)	32× CS 107	Sep 1998	Jan 2012	−0.045 to −1.25[5]	°C		single 1 h		0.1 °C
Soil temperature (1-D), profile (c)	8× CS 107	Aug 2009	…	−0.01 to −1.41[6]	°C	60 s	avg. 1 h		0.1 °C
Soil temperature (1-D), profile (b)	6× PT100	Aug 1999	Aug 2009	−0.02 to −1.43[7]	°C	15 min	avg. 1 h		0.1 °C
Soil heat flux	2× Hukseflux HFP01	Sep 1998	Dec 2012	0.18; 0.24	W m^{-2}		single 1 h		−15 to +5 %
Soil electrical conductivity	TDR Tektronix 1502B, SDM50 multiplexer, 29× TDR triple-wire 0.24 m long probes	Sep 1998	Dec 2009	0 to −1.2	dS m^{-1}		single 1 h		
Soil electrical conductivity	TDR100, SDM50 multiplexer, 7× CS605 probes, triple-wire 0.3 m	Aug 2009	…	−0.01 to −0.89	dS m^{-1}		single 1 h		
Soil liquid volumetric water content	TDR Tektronix 1502B, SDM50 multiplexer, 29× TDR triple-wire 0.24 m long probes	Sep 1998	Dec 2009	0 to −1.2			single 1 h		
Soil liquid volumetric water content	TDR100, SDM50 multiplexer, 7× CS605 probes, triple-wire 0.3 m	Aug 2009	…	−0.01 to −0.89			single 1 h		
Active layer and permafrost temperature	Geoprecision temperature chain with 10 sensors, M-Log	Aug 2009	Sep 2015	0.5; 0; −0.5; −1; −1.5; −2.5; −3.5; −5.5; −7.5; −9	°C		single 1 h		0.2 °C (absolute accuracy)
Generic sensors									
Snow/surface observation	Camera K1	Aug 2013	…	2	px		single 1 h		

[1] Average; [2] from (M/YYYY); [3] Campbell Scientific Ltd.; [4] 50 % transmission points; [5] see Appendix C, Fig. C8; [6] exact heights (m): −0.01; −0.11; −0.21; −0.37; −0.55; −0.71; −0.89; −1.41; [7] exact heights (m): −0.02; −0.05; −0.24; −0.53; −0.93; −1.43.

3.1.2 Wind speed and direction

The wind speed and direction were measured with an R.M. Young propeller anemometer (model 05103). The wind direction and its standard deviation was recorded at hourly (1998–2009) or half-hourly (2009–present) intervals.

3.1.3 Radiation

Net radiation was measured between 1998 and 2009 using a CSI (Campbell Scientific Ltd.) Q7 net radiometer or an NR Lite net radiometer (Kipp & Zonen) and since 2009 with an NR01 four-component sensor (Hukseflux). Changes in the sensor setup were partly due to destruction by reindeer which prompted an improvement of the fence in 2017. A wind correction was performed according to the manufacturer's suggestion for the Q7 and NR Lite net radiometers (Campbell Scientific Ltd.; details in Appendices C and D). An SP 1110 (Skye Instruments) pyranometer was also installed in 1998 and a CG1 (Kipp and Zonen, Appendix C3) downward-looking pyrgeometer (to detect reflected longwave radiation) in 2003. Regular site visits were made during which the pyranometers were checked for condensation, dirt, physical damage or hoar frost. Nevertheless, because the instruments were largely unattended most of the time, we estimate the field accuracy to have been between ±10 % (for the Q7 sensor) and ±20 % (for the NR Lite). Details on the various net radiometer setups and correction are provided in Appendix D.

3.1.4 Rainfall

An unheated and unshielded tipping bucket rain gauge (R M Young, 52203) was installed on a pole in August 1999, with the top of the bucket about 1.6 m above ground level. The instrument measures only liquid precipitation (rainfall) and not winter snowfall. The tipping bucket was regularly checked in summer by pouring a known volume of water into the bucket and by frequent visual inspections for dirt or snow during each site visit. At wind speeds above 12.5 m s^{-1} (hourly or half-hourly average) the rain gauge was found to record precipitation even when there was none, due to vigorous shaking of the pole; these data were flagged accordingly within the data series. Until 2010, precipitation was only recorded as hourly totals, but the provided data set uses 30 min temporal resolution (half-hours are presented as "NaN", since the hourly total is given at full hour). Total daily precipitation figures from a gauge in Ny-Ålesund are available

through the Norwegian Meteorological Institute (formerly www.eklim.no and www.met.en).

3.1.5 Snow depth

The snow depth around the station has been continuously monitored since 1998 with an SR50 sonic ranging sensor (Campbell Scientific Ltd.) and with an additional SR50 sensor at a nearby (about 85 m away; Fig. 2) eddy covariance station since 2006. The sensor recorded raw distance data from the sensor to the object (in this case the ground or snow surface). The data obtained from the sonic sensor were corrected using the speed of sound at 0 °C and the air temperature measured at the Bayelva site, according to the formula provided by the manufacturer (Campbell Scientific Ltd.; Appendix D, Sect. D4). To obtain the snow depth the distance of the sensor from the ground surface was recorded annually and subtracted from the corrected distance data. Snow depths are provided in the data supplement for this paper. Due to seasonal thawing of the ground, the surface can subside over the season (Overduin and Kane, 2006); thus, negative distance rates of a few centimeters are computed (and not set to zero). The data are not removed from the series since the opposite process, frost heave, takes place during fall freeze-back and thus the surface presumably bounces back to the original height (prior to ground thaw and subsidence). Since the ground surface has little or no vegetation cover the signal is returned with a high degree of accuracy (Table 2). An additional snow depth laser distance sensor (Jenoptik SHM30) was installed at the Bayelva site climate tower in August 2013. The data from the three different snow depth sensors were combined to obtain a continuous record and fill any gaps left by the failure of individual instruments (level 2 data containing all original snow data from the three sites merged into one data product can be found in Sect. 4). Any differences in snow depth between these sensors may therefore be due to microtopographic and microclimatic variations between these two locations.

3.1.6 Time lapse photography of snow cover

In order to monitor the timing and pattern of snow cover changes an automated camera system (K1; Umwelt- und Ingenieurtechnik, Dresden) was set up in August 2013 to photograph the land surface in those areas in which the instruments were located (Fig. C2). The camera recorded one image every hour; during the polar night a light was switched on automatically while each image was being recorded.

3.1.7 Dielectric number of snow

The dielectric number (also referred to as relative permittivity) of the snow was measured using a vertically installed time-domain reflectometry (TDR) probe. The length of the TDR probe was 0.5 m between 1998 and 2007 and 0.33 m from 2009 onwards. Dielectric numbers are provided in the data set for both the snow-covered and the snow-free periods (recording only air dielectric numbers). When the snow cover depth exceeds the length of the TDR probe the dielectric number data can be used to infer dry snow densities using empirical relationships (Schneebeli et al., 1998). In wet snow, the measured snow dielectric number can be used for the calculation of the snow liquid water content using the composite approach with ice added as an additional phase (e.g., Roth et al., 1990) and measured snow densities (Appendix E, Table E1).

3.1.8 Vertical profiling of the physical properties of snow

Snow depth and vertical profiles for temperature, density and dielectric numbers were collected from the site and surrounding areas during a number of end-of-snow (spring) seasons. These profiles, which were collected at irregular intervals between 2000 and 2016, provide additional information on the snowpack. They typically reveal the presence of a number of ice layers (including a basal ice layer) and snow densities of between 220 and 440 $\mathrm{kg\,m^{-3}}$. The typical end-of-spring average snow density before snow melts is 350 $\mathrm{kg\,m^{-3}}$. The end-of-spring season snow water equivalent varies between the years due to variations in snow depth (Fig. 3). Details of these profiles, including some stratigraphic information, are provided in Appendix E (Table E1).

3.2 Subsurface data on permafrost and the active layer

Data have been collected from a variety of installations that were changed over time because of the deterioration of sensors or disturbance by reindeer. As a result, there are a number of data series from different profiles rather than one continuous data series. Some measurements were also discontinued (e.g., soil heat flux).

3.2.1 Instrument installation and soil sampling

In order to take into account any possible effects of small variations in vegetation and microtopography at the site (e.g., due to the presence of non-sorted circles), instruments were installed in a number of different positions within a profile. Deterioration of data quality and the failure of some sensors also led to the installation of new sensors in new profiles.

Instrument installation and soil sampling 1998

The first set of instruments was installed in 1998, within one of the non-sorted circles (Appendix C, Fig. C7), for which a trench 2 m wide and 1.4 m deep was excavated across the circular feature (Appendix C, Fig. C8). The surface was carefully cut and the excavated soil stockpiled separately according to depth and soil horizon, in order to be able to restore the original profile following installation of the instruments. The unfrozen layer was 1.2 m deep at the time of installation. The

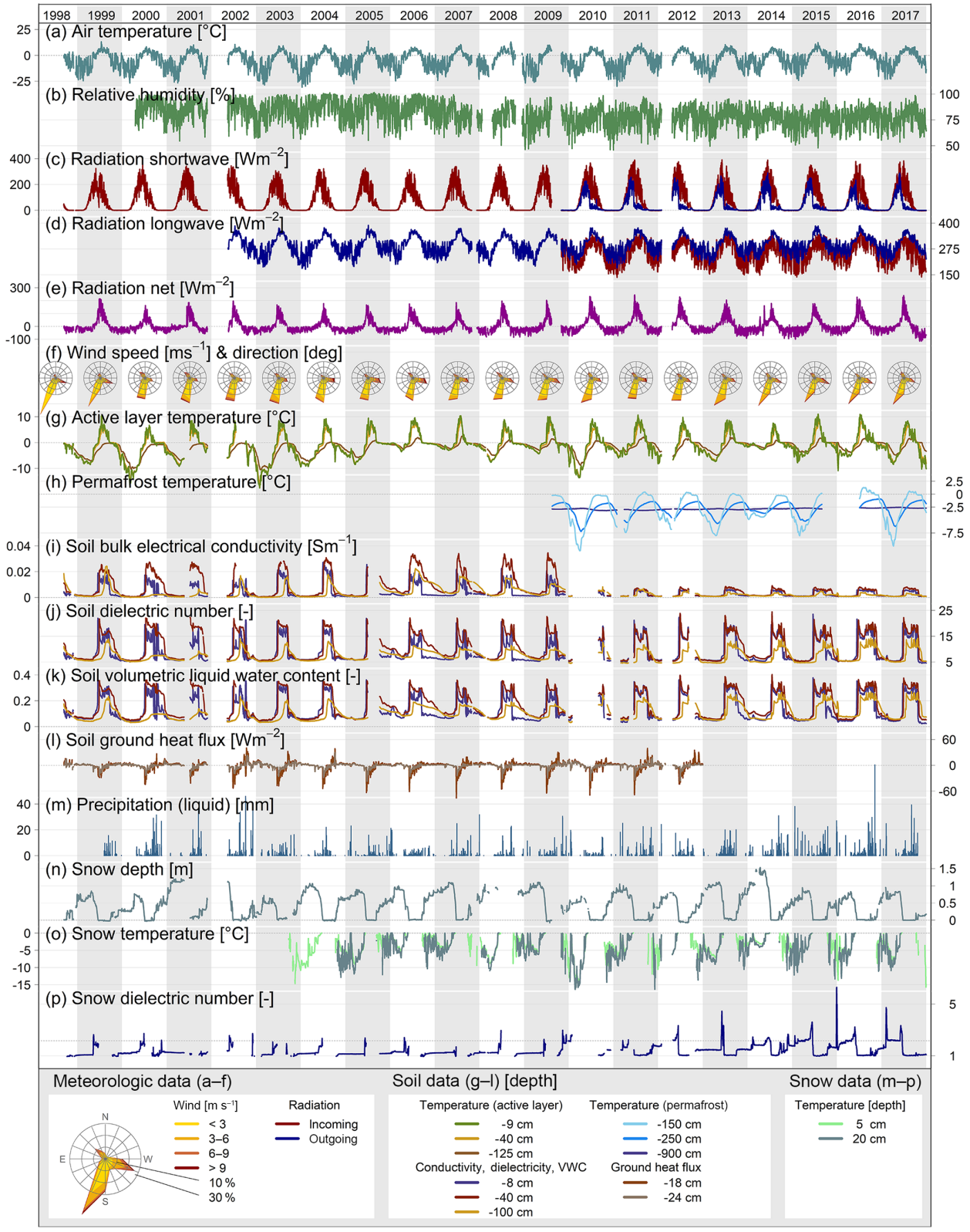

Figure 3. Time series of Bayelva data provided in this paper. **(a)–(f)** meteorological data, **(g)–(l)**: soil and subsurface data, **(m)–(p)**: snow data. The data are organized following the structure of Appendix G. Further details on the sensors and periods of operation are given in Table 2. This plot (divided in three parts for better visibility) is also provided in Appendix H.

entire profile was quite heterogeneous but consisted mainly of silty clay, with a stone content of less than 10 %. The stone content increased to about 50 % in a slightly inclined layer approximately 20 cm thick that occurred at a depth of 50 cm; the stones were quite large (including cobbles in excess of 6 cm in diameter) but showed no preferred orientation. Below 85 cm depth the soil was coal-rich and contained massive coal lenses.

Sensors were installed in the undisturbed wall of the soil pit (Appendix C, Fig. C8b) to obtain an instrumented cross section of the pedon. The pit was then backfilled. Soil samples were collected during the installation so that physical parameters could be analyzed. The stratigraphic and textural information from the soil profile, including soil organic carbon (C), nitrogen (N) and sulfur (S) concentrations, can be found in Appendix F.

Soil sampling 2007

A number of additional soil profiles in the vicinity of the Bayelva site were sampled in 2007 (Fig. 2). Data for the soil texture; bulk density; and carbon, nitrogen and sulphur (C, N, S) content of these profiles is also included in Appendix F (Table F1).

Instrument installation and soil sampling 2009

A new set of measurement profiles was established within a second non-sorted circle close to the 1998 profiles (Appendix C, Fig. C9). The site was chosen for its similarity to the 1998 site, in order to provide an analogous continuation of the long-term subsurface data from the 1998 profiles. Data on the soil texture; its bulk density; and carbon, nitrogen and sulphur content can be found in Appendix F.

All profiles show cryoturbation features at the surface through patterned ground (non-sorted circles) and also within the soil profile, e.g., roots that are transported downwards through cryoturbation (Figs. C8 and C9).

3.2.2 Ground temperature

Soil profile sensor installation 1998

Pairs of soil temperature and soil water content sensors were installed over a cross section in 1998; their positions are shown in Appendix C (Fig. C8). The probes automatically recorded temperatures from that time until January 2012. The temperatures were measured using CSI (Campbell Scientific Ltd.) thermistors connected to a CR10X data logger with an AM416 multiplexer. The voltage measured for each sensor was stored in a database. Temperatures were calculated from the raw data using the Steinhart–Hart equation (Steinhart and Hart, 1968) and sensor calibration at 0 °C (Table D2). The average accuracy determined through calibration was 0.01 °C with a precision better than 0.002 °C. However, the max deviation at 0 °C was 0.1 °C. After installation, the sensors cannot be recalibrated, certainly not without a lasting physical disturbance of the profile. However, temperatures during spring thaw and fall refreezing are stable at the phase change temperature (the zero-curtain effect in permafrost soils). Assuming that freezing point depression (i.e., soil type and soil water composition) does not change significantly from year to year, these periods can be used to evaluate sensor stability. During the first 2 years (1998–1999) the temperatures during these periods were stable to within 0.1 °C. Subsequently, temperature readings from 9 of the 32 sensors started to drift and showed a positive offset relative to the ∼ 0 °C zero-curtain period. The temperature sensor at, for example, 19 cm depth showed correct temperatures during the fall freeze-back of 1998 and 1999, but in the fall of 2000 the measured soil temperatures shifted to positive values by 0.5 °C (offset from the fall zero-curtain). This offset increased further to about 6 °C in 2009. All sensors with temperature offsets of 0.5 °C or more were flagged accordingly within the data set. The positive temperature offset was most likely due to additional resistance, either in the cables due to leakage currents or in the multiplex due to corrosion. In addition to the temperature offset, the data quality of the years 2002 to 2007 was strongly affected by irregular spikes caused by the multiplexer. In the worst year, 2002, these spikes occurred for 5 to 7 % of all measured values in all soil temperature series of the 2-D profile. Spikes were flagged automatically and manually within the data set. The external charge controller regulating the solar and wind energy supply was changed in 2002 following a power failure, resulting in increased noise levels in the measured temperatures between 2002 and 2012 and the subsequent discontinuation of this data series.

Soil profile sensor installation 1999

Temperature sensors were installed in 1999 in one additional vertical profile, 2 m apart, within the fenced-off area, below vegetation (Appendix C, Fig. C6b). A small-diameter (vertical) hole was drilled by a hand drill into the ground in the fall of 1999. The PT100 temperature sensors were calibrated in ice-slush water for at least 12 h to determine the offset at 0 °C. The max deviation at 0 °C was 0.1 °C. Similar to the 107 probes, the average accuracy determined through calibration was 0.01 °C with a precision better than 0.002 °C. Wooden sticks to which sensors had been attached were then inserted into the holes down to 1.50 m into the permafrost beneath the active layer in such a way that the sensors formed a tight fit in the hole and no air was able to pass. The temperature sensors were attached at regular intervals to bamboo sticks. The upper sensors were affected on 11 September 2003 by reindeer disturbance. Furthermore, the upper two sensors moved upwards by about 10 cm between 2003 and 2016 due to frost heave and they were removed from the data series.

Soil profile sensor installation 2009

Pairs of soil temperature (CS107) and water content (TDR) probes were installed during August 2009, close to the first profile that was installed in 1998 (Appendix C, Fig. C9). Soil temperatures were measured at 11 depths in a profile from the surface down to a depth of 1.4 m. The data quality from the 2009 system improved considerably compared to the 1998 system, probably due to the data logging and multiplexer system used (CR10X from 1998 to 2011; CR1000 since 2009). Data collection is ongoing.

3.2.3 Soil dielectric number, volumetric liquid water content and bulk electrical conductivity

Soil profile sensor installations 1998 and 2009

Time-domain reflectometry probes were installed horizontally adjacent to the temperature probes installed in soil profiles in 1998 and 2009 (see above and Appendix C, Table C5).

These TDR probes automatically recorded hourly measurements of bulk electrical conductivity (BEC) and the dielectric number (also referred to as relative permittivity), obtained by measuring the amplitude at very long times and the L_a/L ratio (ratio of the apparent to real probe length, corresponding to the square root of the dielectric number). From 1998 to 2008 the measurements were obtained using a Tektronix 1502B cable tester connected to a CR10X data logger and custom-made triple-wire 24 cm probes. Since 2009 a CSI TDR100 reflectometer has been used, connected to a CR1000 data logger and 30 cm TDR CS605 probes (Campbell Scientific Ltd.). All TDR probes were calibrated for probe offset following the method described in Heimovaara and de Water (1993) and the CSI TDR 100 manual (http://www.campbellsci.de/tdr100). The dielectric number data and computed volumetric liquid water in frozen and unfrozen soil are provided with the data set. The calculation for volumetric liquid water content takes into account four phases of the soil medium (air, water, ice, mineral) and uses the mixing model from Roth et al. (1990; Appendix D, Sect. D1).

Time-domain reflectometry can also be used to measure the impedance Z (Ω) of the bulk soil, which is related to the soil's bulk electrical conductivity. These data were used to infer the electrical conductivity of soil water and solute transport in the non-sorted circle over a period of 1 year (Boike et al., 2008a). The impedance can be determined from the attenuation of the electromagnetic wave traveling along the TDR probe after all multiple reflections have ceased and the signal stabilized. The bulk electronic conductivities were recorded hourly using the TDR setup described in this section. The equipment installed in 1998 was calibrated in pure water, in air and in NaCl solutions with various known conductivities and is corrected for temperature (25 °C), following the method by Heimovaara et al. (1995). The TDR equipment installed in 2009 was not calibrated for BEC and a probe constant of 1 was used for BEC waveform retrieval; Campbell Scientific Ltd. suggests a probe constant (K_p) for the CS605 probes of 1.74. The lack of calibration explains the differences of the data sets recorded between the time 1998–2009 and 2009 to present (Fig. 3i). Measurements of electric conductivity and the dielectric number were affected by irregular spikes and possibly by sensor drift similarly to the soil temperature measurements. Spikes were flagged automatically and manually, while drifts could not be flagged due to the lack of reference data. Overall, the quality of soil data instrumented in 1998 is of reduced quality since July 2005. Values for dielectric number, computed volumetric liquid water content and bulk soil electrical conductivity can be found in the data set.

3.2.4 Soil heat flux

Two heat flux plates (Hukseflux HFP01), one installed at 0.18 m depth below the unvegetated center of the non-sorted circle and the second at 0.24 m depth below the vegetated rim of the non-sorted circle, recorded ground heat flux between September 1998 and September 2009 (Fig. 3). The manufacturer's calibration values were used to record heat flux in $W\,m^{-2}$.

3.2.5 Permafrost and active layer temperature

A 9.3 m borehole was drilled using a rotary drill rig on 30 March 2009 and cased with PVC. No stratigraphic information or drill core was recovered. A thermistor string was installed, with one sensor above the ground surface and nine from the surface down to 9 m depth (at 0, 0.5, 1.0, 1.5, 2.5, 3.5, 5.5, 7.5 and 9 m below ground surface, Appendix C, Fig. C10). The casing was left open (not refilled) so that the thermistor chain could be retrieved or replaced. Because of instrument failure, thermometers were retrieved and replaced several times. From August 2009, a Geoprecision M-Log5W data logger and sensor chain were used. Temperatures were recorded at hourly intervals, with no averaging; no data was recorded between 30 January and 29 March 2011, due to a low battery voltage. Geoprecision claims an accuracy of ±0.05 °C (at 0 °C) and a resolution of 0.01 °C, which is suitable for measurements in the range from −50 to +120 °C. However, comparison measurements using a PT100 thermometer at the same depths in the borehole showed a deviation of up to 0.2 °C. In 2014, a wooden shield was installed over the casing to prevent warming due to radiation and to facilitate natural ventilation (Appendix C, Fig. C10). Caution is warranted when using the borehole temperatures in the uppermost 1–2 m, since they may be affected by air movement in the borehole. These data are flagged in the data series.

Table 3. Description of data level and quality control for data flags. Most flags are run automatically; few are done manually (e.g., three for maintenance, six for plausibility).

Flag	Meaning	Description
ONL	Online data	Data from online stations, daily download, used for online status check
RAW	Raw data	Base data from offline stations, 3-monthly backup of online data, used for maintenance check in the field
LV0	Level 0	Standardized data with equal time steps, without gaps and in a standard data format
LV1	Level 1	Quality-controlled data including flags; quality control includes maintenance periods, physical plausibility, spike and constant value detection, sensor drifts and snow-on-sensor detection
LV2	Level 2	Modified data compiled for special purposes such as combined data series from multiple sensors and gap-filled data
0	Good data	All quality tests passed
1	No data	Missing value
2	System error	System failure led to corrupted data; e.g., when the power supply broke down, sensors were removed from their proper location, sensors broke or the data logger saved error codes
3	Maintenance	Values influenced by the installation, calibration and cleaning of sensors or programming of the data logger; information from field protocols of engineers
4	Physical limits	Values outside the physically possible or likely limits; e.g., relative humidity should be in a range of 0–100 %
5	Gradient	Values unlikely because of prolonged constant periods or high or low spikes; test within each single series
6	Plausibility	Values unlikely in comparison with other series or for a given time of the year; flagged manually by engineers
7	Decreased accuracy	Values with decreased sensor accuracy, e.g., identified when freezing soil does not have a temperature of 0 °C
8	Snow covered	Good data, but the sensor is snow covered

4 Data quality control and availability

The primary purpose of quality control of observational data is to detect missing data, errors in the data, and possibly to correct errors in order to ensure the highest possible standard of accuracy and optimal use of the data by the broadest range of possible users. We differentiate between different data levels, from online data (http://www.awi.de/im-fokus/permafrost/direkter-draht-in-den-permafrost.html) to level 2 data (Table 3). Data supplied with this paper are level 1 and level 2 data. Level 1 data have undergone an extensive quality-control and are flagged with regards to maintenance periods, physical plausibility, spike and constant value detection and sensor drifts (Table 3). Level 2 data are compiled for special purposes such as a combination of data series from multiple sensors and gap-filling of data (documentation of source data is supplied in the PANGAEA data archive). Examples in this paper of level 2 data are the snow cover, soil temperature and soil volumetric water content data series that have been combined from various stations into a single data series, in order to obtain a long-term picture. There are eight quality control types (Table 3). These flags include information on the system's maintenance; no data availability; system error; and on consistency checks based on physical limits, gradients and plausibility. Due to the failure of some sensors that cannot be retrieved for repair or recalibration (e.g., sensors installed in the ground), the initial accuracy and precision of the sensors is not maintained.

In the case of soil temperature, the accuracy can be estimated by analysis of temperatures relative to the fall zero-curtain effect assuming soil water composition is similar from year to year. As an example, our temperature data have been checked through the fall zero-curtain effect and thus provide information on any reduction in accuracy (see Table 3, Flag 7). These checks are mandatory when small warming trends are to be estimated and interpreted. The selection of flagged data depends on its application and the required accuracies.

The data from this Bayelva site have been widely used for the development and evaluation of land surface models (e.g., Chadburn et al., 2017; Ekici et al., 2014, 2015). The newly collated data set will allow multi-year model runs, with improved quality control and checks. The data set presented herein is freely available, either as a download from

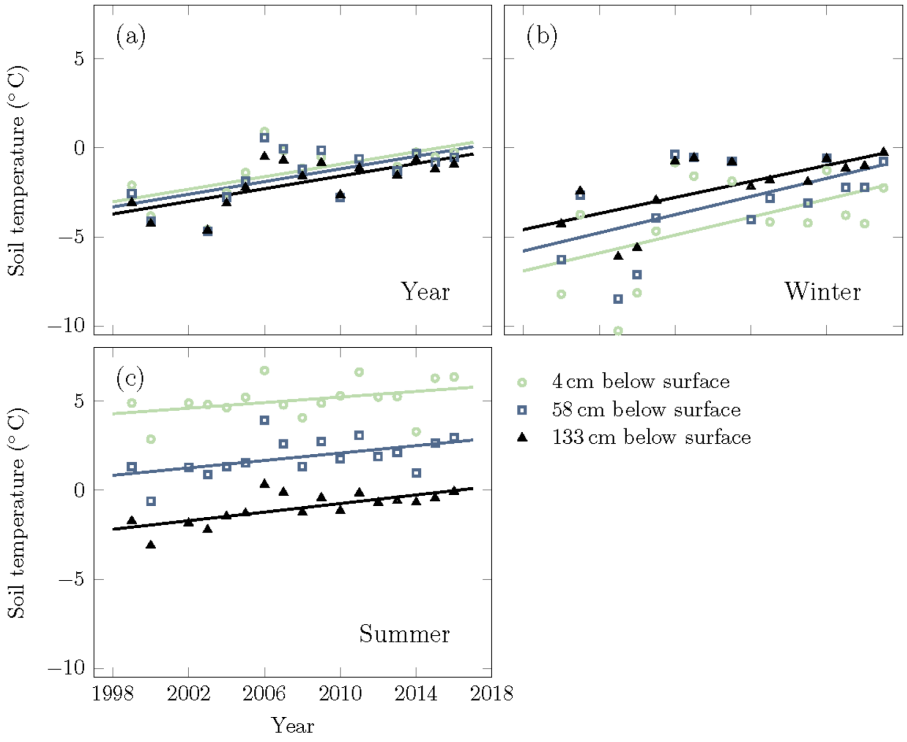

Figure 4. Bayelva mean 20-year temperature increases for three depths from September 1998 to September 2017 using level 2 soil temperatures. **(a)** In the active layer (4 and 58 cm) and in the top of permafrost (138 cm): $0.18 \pm 0.07\,°C\,year^{-1}$; **(b)** in winter (December, January, February): 0.25 ± 0.12, 0.25 ± 0.11 and $0.23 \pm 0.07\,°C\,year^{-1}$, respectively; and **(c)** in summer (June, July, August): 0.08 ± 0.05, 0.10 ± 0.04 and $0.12 \pm 0.03\,°C\,year^{-1}$, respectively. Years in which data gaps of more than 48 h exceeded 5 % of data were included; data gaps were interpolated linearly.

PANGAEA (https://doi.org/10.1594/PANGAEA.880120) or from the Supplement of this paper. The data are provided as ASCII files. Other available data sets include a flux data set in the European Fluxnet database (Lüers and Boike, 2013) and aerial imagery of the snow cover (Westermann et al., 2015). Volumetric soil liquid water content and snow cover data are transferred in real time to the NASA SMAP mission (https://smap.jpl.nasa.gov/) and are uploaded to the PANGAEA archives on an annual basis.

5 Data availability

The entire data set is available through the following data provider and links:

- https://doi.org/10.1594/PANGAEA.880120 (time series)
- https://doi.org/10.1594/PANGAEA.884730 (HRSC-AX data products)
- https://zenodo.org/record/1139714 (time series)
- https://zenodo.org/record/1145373 (HRSC-AX data products)

The time series data are also available through the supplement of this ESSD paper.

6 Outlook

Permafrost around the Arctic is warming and thawing (Christiansen et al., 2010; Romanovsky et al., 2008), and this is true for Svalbard (Isaksen et al., 2007b) and the Bayelva site as well. The record from 2009 to 2017 of permafrost temperature measurements shows a zero-amplitude depth of 5.5 m at a mean temperature of −2.8 °C. Mean annual, summer and winter soil temperature data at all depths have been rising over the period of record (Fig. 4, three depths are shown) as well as in the deeper permafrost (Fig. 3h). Interannual to subdecadal variability is evident in the data and results mostly from differences during the winter months. Future analysis is required to detangle the relationship between potential meteorological drivers and permafrost degradation at this site. The data set described and distributed in this paper provides a basis for analyzing this relationship at one site and a means of calibrating earth system modeling efforts over a long observational period. Developing predictive capacity for permafrost warming will be key to understanding the role of the permafrost feedback in the global climate system.

Appendix A: Symbols and abbreviations

R_T	measured resistance
δ_o	resistance offset at 0 °C
L_a/L	apparent length of the TDR probes (TDR data logger output)
ε_b	bulk dielectric number (Ka), also referred to as relative permittivity
ε_l	temperature-dependent dielectric number of liquid water
ε_i	dielectric number of ice
ε_s	dielectric number of soil matrix
ε_a	dielectric number of air
θ_l	volumetric liquid water content
θ_i	volumetric ice content
θ_s	volume fraction of soil matrix
θ_a	volume fraction of air
θ_{tot}	total volumetric water content (liquid water and ice)
α	geometry of the medium in relation to the orientation of the applied electrical field (see Roth et al., 1990)
Φ	porosity
Z	impedance
BEC	bulk electrical conductivity
Dsn	snow depth (m)
RadNet	net radiation ($W\,m^{-2}$)
$RadNet_{raw}$	uncorrected net radiation ($W\,m^{-2}$)
Vwind	wind speed ($m\,s^{-1}$)
TOC	total organic carbon (%)
SOCC	soil organic carbon content ($kg\,m^{-2}$)
CD_{bulk}	bulk carbon density ($kg\,m^{-3}$)
ρ_{bulk}	average dry bulk density ($kg\,m^{-3}$)
z	layer thickness (m)

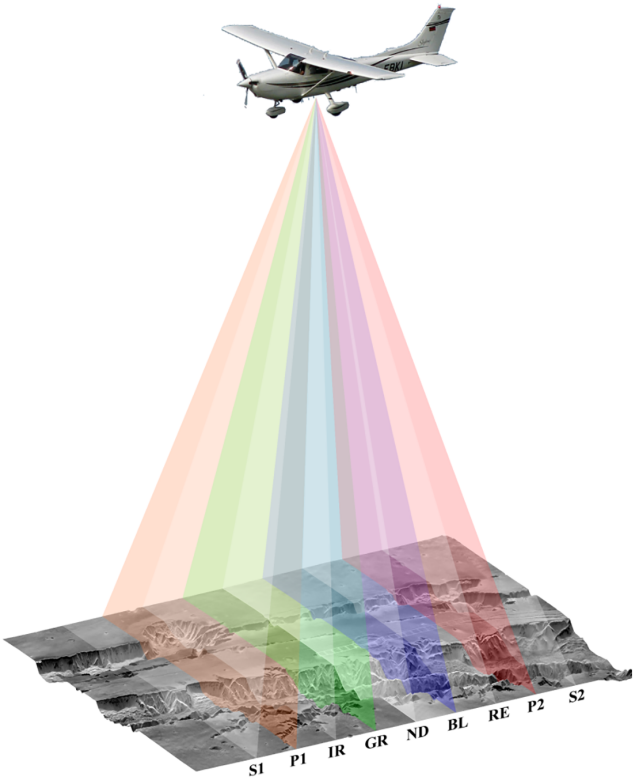

Figure B1. Operating principle of the airborne high-resolution stereo camera (HRSC-AX), and viewing geometry of the individual charge-coupled device (CCD) sensors. ND – nadir channel; S1 and S2 – stereo 1 and stereo 2; P1 and P2 – photometry 1 and photometry 2; IR – near-infrared channel; GR – green channel; BL – blue channel; RE – red channel. All nine line sensors have a cross-track field of view of ±6°.

Appendix B: Description of HRSC-AX images

HRSC is a multisensor pushbroom instrument with nine charge-coupled device (CCD) line sensors mounted in parallel (Fig. B1) that has been in orbit around Mars since January 2004 on ESA's Mars Express spacecraft (Gwinner et al., 2016). It simultaneously obtains high-resolution stereo, multicolor and multiphase images. Digital photogrammetric techniques are used to reconstruct the topography on the basis of five stereo channels, which provide five different views of the ground.

The four color channels (blue, green, red and near-infrared; Fig. B2) are used to make true orthophotos in color and false color. The particular value of HRSC is the stereo capability, which allows the systematic production of high-resolution digital elevation models (DEMs) with grid sizes between 50 and 100 m (Wewel et al., 2000; Scholten and Gwinner, 2004; Scholten et al., 2005; Gwinner et al., 2005, 2010).

Since 1997 different airborne versions of HRSC have been developed, one of which (HRSC-AX) was used to acquire

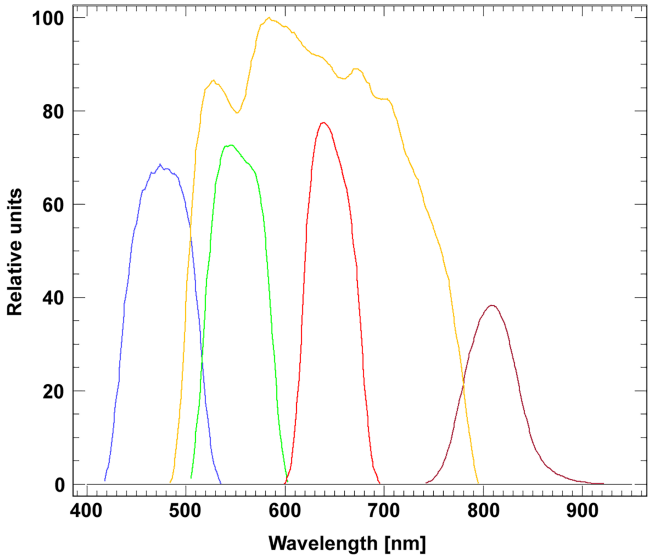

Figure B2. Spectral response of HRSC-AX panchromatic color filters.

stereo color images over Svalbard. The principles of HRSC-AX data processing are described by Gwinner et al. (2006). Data on the camera orientation are reconstructed from a global positioning system inertial navigation system (GPS INS). HRSC-AX has been used in diverse technical and scientific applications (e.g., Gwinner et al., 1999, 2000). The aerial survey covering the Brøgger peninsula took place on 17 July 2008 at around noon, acquiring data over most of the northern part of Brøggerhalvøya (Fig. B3). A Dornier Do 228 aircraft from the German Aerospace Center (DLR) was used for the survey, flying at an altitude of ∼2800 m. A comprehensive description of the initial results is given by Hauber et al. (2011a, b).

Data processing from the raw images to the final data products, including digital photogrammetric processing, was performed with the VICAR (Video Image Communication and Retrieval; http://www.mipl.jpl.nasa.gov/external/vicar.html) software developed at the JPL (Jet Propulsion Laboratory, Pasadena, USA) and the DLR. We provide HRSC-AX data in the form of a digital elevation model and as individual channels (panchromatic nadir channel; red, green, and blue color channels; and CIR, color-infrared, false-color channels). The CIR channels are computed by merging a false-color image (an RGB image where R, G and B correspond to the original infrared, red and green channels, respectively) with the nadir channel. Table B1 lists important key properties of the individual HRSC-AX image files. Metadata for HRSC-AX data are contained in "image labels", which we provide as two XML files (one for the panchromatic and (false) color images, and one for the DEM). The label entries consist of keyword-value pairs; essential keywords are defined below in Table B2. The elevations recorded in the DEM are ellipsoid heights; i.e., they are not computed with respect to

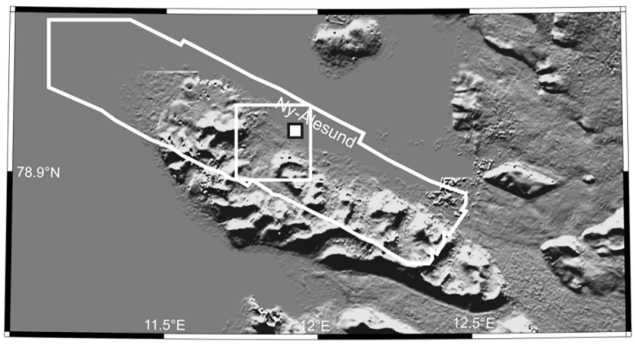

Figure B3. Context map of the Brøgger peninsula, with the thick white outline showing the total coverage of the HRSC-AX survey and with the white square indicating the location of the image tile provided in this publication (base map: hillshade version of ASTER DEM).

a geoid but to a mathematically defined reference surface, which is a rotational ellipsoid with the equatorial A and B axes both having a radius of 6378.14 km and the polar C axis having a radius of 6356.75 km. This results in an offset of about 36.5 m with respect to geoid heights; i.e., sea level in the HRSC-AX DEM is not at 0 m, but at ∼ 36.5 m.

Table B1. Image size and pixel size of individual HRSC-AX images.

Image name	Number of lines	Number of samples	Ground pixel size
430-8765_5.0x5.0km.pan	25 000	25 000	0.2 m
430-8765_5.0x5.0km.dsm	10 000	10 000	0.5 m
430-8765_5.0x5.0km.re	25 000	25 000	0.2 m
430-8765_5.0x5.0km.gr	25 000	25 000	0.2 m
430-8765_5.0x5.0km.bl	25 000	25 000	0.2 m
430-8765_5.0x5.0km.cir_re	25 000	25 000	0.2 m
430-8765_5.0x5.0km.cir_gr	25 000	25 000	0.2 m
430-8765_5.0x5.0km.cir_bl	25 000	25 000	0.2 m

Table B2. Description of metadata (keyword-value pairs) contained in the HRSC-AX image headers.

Name	Definition	Dimension	Type	Label Group
File_Name	Name of the data file		string	
FORMAT	Image format (i.e., range of gray values or digital numbers: byte = 8 bit per pixel, half = 16 bit per pixel, real = 32 bit per pixel)		string	
TYPE	Type of data file		string	
ORG	Order of image file (BSQ = band sequential)		string	
NL	Number of lines		int	
NS	Number of samples		int	
NB	Number of bands		int	
TARGET_NAME	Name of the target		string	MAP
A_AXIS_RADIUS	The A_AXIS_RADIUS element provides the value of the semi-major axis of the ellipsoid that defines the approximate shape of a target body. "A" is usually in the equatorial plane.	km	real	MAP
B_AXIS_RADIUS	The B_AXIS_RADIUS element provides the value of the intermediate axis of the ellipsoid that defines the approximate shape of a target body. "B" is usually in the equatorial plane.	km	real	MAP
C_AXIS_RADIUS	The C_AXIS_RADIUS element provides the value of the C_AXIS of a solar system body. For triaxial ellipsoidal objects, the C_AXIS is the semiminor axis of the ellipsoid which defines the approximate shape of the body.	km	real	MAP
BODY_LONG_AXIS_LONGITUDE	The BODY_LONG_AXIS_LONGITUDE element represents the offset between the longest axis of the triaxial ellipsoid used to model a body and the prime meridian of the body. Its value is the sum of the offset added to the prime meridian. This term is the positive west longitude, measured from the prime meridian.	deg	real	MAP
CARTESIAN_AZIMUTH	The CARTESIAN_AZIMUTH element provides the clockwise rotation, in degrees, of the line and sample coordinates with respect to the center of the pixel at the map projection origin (i.e., where LINE_PROJECTION_OFFSET and SAMPLE_PROJECTION_OFFSET are measured).	deg	real	MAP
CENTER_LATITUDE	The CENTER_LATITUDE element provides a reference latitude for certain map projections. In many projections, the CENTER_LATITUDE along with the CENTER_LONGITUDE defines the point or tangency between the sphere of the planet and the plane of the projection.	deg	real	MAP
CENTER_LONGITUDE	The CENTER_LONGITUDE element provides a reference longitude for certain map projections. In many projections, the CENTER_LONGITUDE along with the CENTER_LATITUDE defines the point or tangency between the sphere of the planet and the plane of the projection.	deg	real	MAP
COORDINATE_SYSTEM_NAME	Defines whether the CENTER_LATITUDE is geocentric or geodetic.		string	MAP
LINE_PROJECTION_OFFSET	The LINE_PROJECTION_OFFSET element provides the line offset value of the map projection origin position from the center of the pixel at line and sample position 1, 1 (line and sample 1, 1 is considered the upper left corner of the digital array).	pixel	real	MAP
SAMPLE_PROJECTION_OFFSET	The SAMPLE_PROJECTION_OFFSET element provides the sample offset value of the map projection origin position from the center of the pixel line and sample 1, 1 (line and sample 1, 1 is considered the upper left corner of the digital array).	pixel	real	MAP
MAP_PROJECTION_TYPE	The MAP_PROJECTION_TYPE element identifies the type of projection characteristic of a given map.		string	MAP

Table B2. Description of metadata (keyword-value pairs) contained in the HRSC-AX image headers.

Name	Definition	Dimension	Type	Label Group
MAP_SCALE	The MAP_SCALE element identifies the scale of a given map. The scale is defined as the ratio of the actual distance between two points on the surface of the target body to the distance between the corresponding points on the map. The MAP_SCALE references the scale of a map at a certain reference point or line. Certain map projections vary in scale throughout the map. In general, the MAP_SCALE usually refers to the scale of the map at the CENTER_LATITUDE and CENTER_LONGITUDE.	km pixel^{-1}	real	MAP
POSITIVE_ LONGITUDE_ DIRECTION	The POSITIVE_LONGITUDE_DIRECTION element identifies the direction of longitude (e.g., east, west) for a planet. The IAU definition for direction of positive longitude is adopted.		string	MAP
SPHERICAL_ AZIMUTH	One of three Euler angles (the others are CENTER_LATITUDE and CENTER_LONGITUDE) that define the pre-mapping orientation of the planetary sphere for any spherical projection.		real	MAP
DTM_RANGE	Indicates at which minimum or maximum value the elevations in the DTM raster file have been cut off.		real (2)	H
DTM_A_AXIS_RADIUS	The DTM_A_AXIS_RADIUS element provides the value of the $(+X)$ semi-axis length of the triaxial ellipsoid surface used as reference for DTM data.	km	real	DIGITAL_ TERRAIN_ MODEL
DTM_B_AXIS_RADIUS	The DTM_B_AXIS_RADIUS element provides the value of the $(+Y)$ semi-axis length of the triaxial ellipsoid surface used as reference for DTM data.	km	real	DIGITAL_ TERRAIN_ MODEL
DTM_C_AXIS_RADIUS	The DTM_C_AXIS_RADIUS element provides the value of the $(+Z)$ semi-axis length of the triaxial ellipsoid surface used as reference for DTM data.	km	real	DIGITAL_ TERRAIN_ MODEL
DTM_OFFSET	The DTM_OFFSET element provides the constant value by which a stored elevation value is shifted or displaced.	m	real	DIGITAL_ TERRAIN_ MODEL
DTM_SCALING_ FACTOR	The DTM_SCALING_FACTOR element provides the constant value by which the stored elevation is multiplied.		real	DIGITAL_ TERRAIN_ MODEL
DTM_DESC	The DTM_DESC provides a free form, unlimited-length character string that describes the DTM data.			DIGITAL_ TERRAIN_ MODEL

Appendix C: Metadata description and pictures of climate, soil and permafrost stations, and instruments

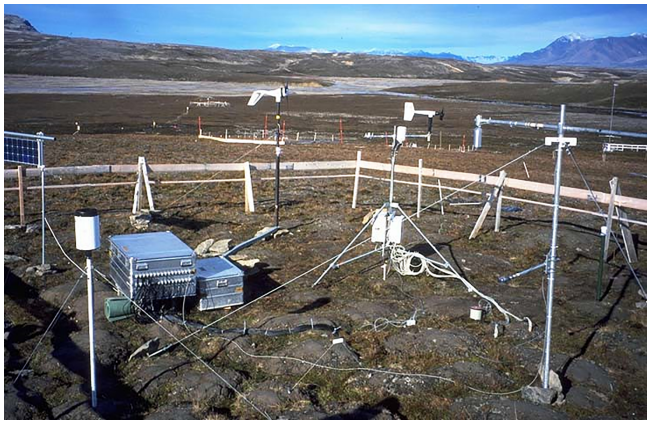

Figure C1. Bayelva climate station setup, September 1998–August 2009, (78.92094° N, 11.83334° E). Picture taken after installation in August 1998.

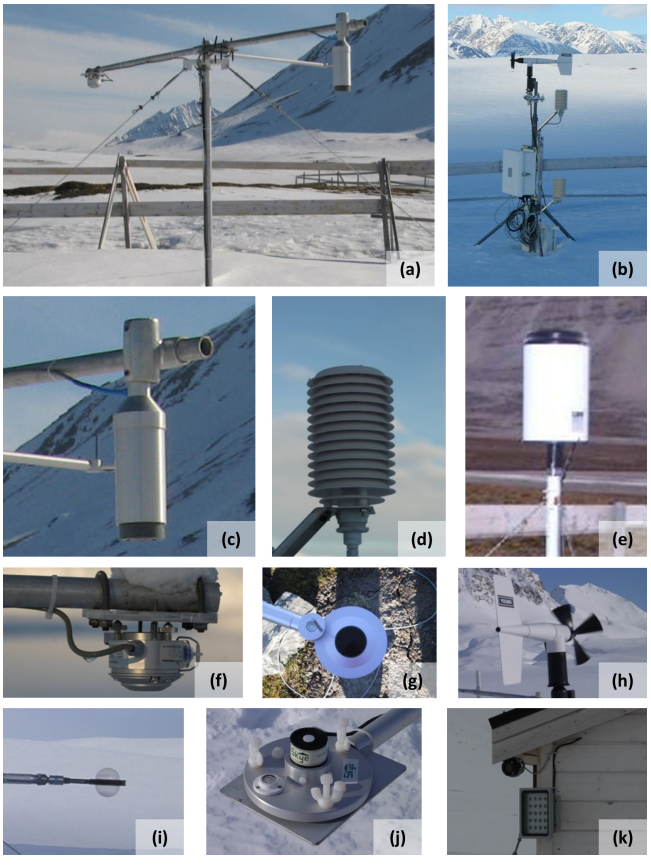

Figure C2. Climate station, Bayelva, September 1998–August 2009. **(a)** Radiation–snow tower, **(b)** meteorological tower, **(c)** snow height sensor (from September 1999: 2 m; from July 2001: 1.6 m; from September 2003: 1.45 m), **(d)** temperature–relative humidity (2 m) and temperature (1 m) sensor, **(e)** rain gauge (1.68 m top of bucket above ground level), **(f)** pyrgeometer (from May 2003: 2 m; from September 2003: 2 m) installed in May 2002, **(g)** net radiometer (from April 2000: 1.14 m; from September 2003: 1.6 m), **(h)** wind speed and wind direction sensor (3 m), **(i)** net radiation sensor (from April 2000: 1.14 m, from September 2003: 1.6 m), **(j)** pyranometer (2 m) and **(k)** camera (2 m) with flash since August 2013. Sensor details can be found in Table 2.

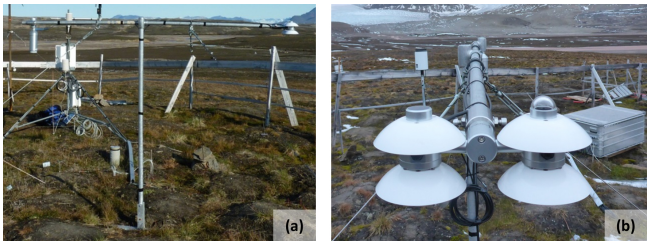

Figure C3. Climate station, Bayelva, October 2009–present (with sensor heights), (78.92094° N, 11.83334° E). **(a)** radiation–snow tower; **(b)** four-components radiation (1.56 m).

Figure C4. Laser snow depth sensor attached to the climate station, Bayelva, August 2013–present, (78.92094° N, 11.83334° E).

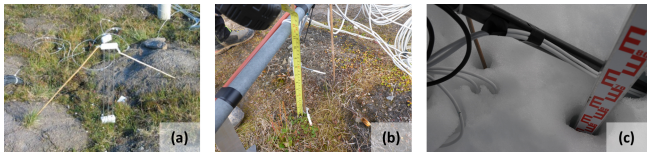

Figure C5. **(a)** Vertically installed time-domain reflectometry (TDR) air–snow TDR probe (50 cm length) above the ground surface during summer at the Bayelva climate station (1999). During winter (fully snow covered), the dielectric number of snow is recorded. **(b)** PT100 temperature sensors in air (summer) at 4 and 20 cm above ground surface. **(c)** PT100 temperature sensors in snow (winter) with air gaps around cables and sticks; the TDR probe is completely covered with snow and not visible from the surface.

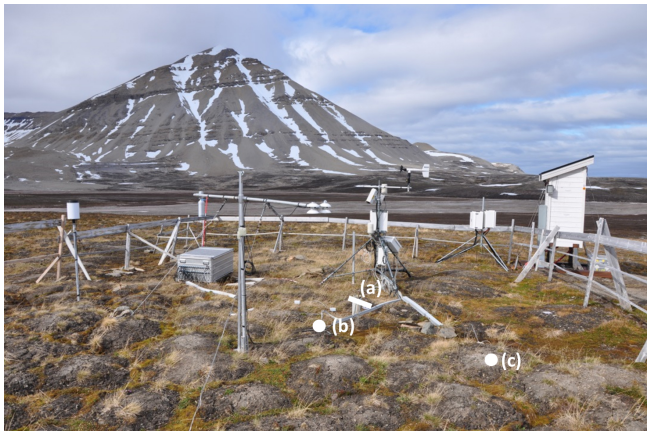

Figure C6. Location of soil profiles, Bayelva, 1998, 1999 and 2009, (78.92094° N, 11.83334° E). **(a)** The 2-D soil profile and station location 1998 (installed August 1998), **(b)** 1-D soil station 1999 (installed July 1999), and **(c)** 1-D soil profile and station 2009 (installed August 2009).

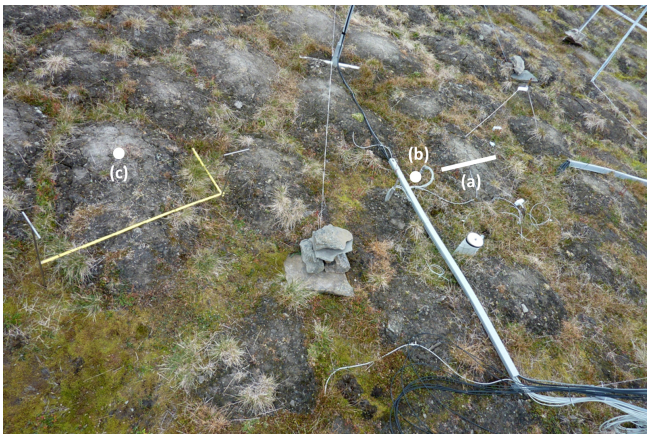

Figure C7. Soil profile and station location **(a)** 1998, **(b)** 1999 and **(c)** 2009. **(b)** Upper temperature sensors were affected by reindeer disturbance in September 2003. Furthermore, the temperature sensors were affected by continuous frost heave by about 10 cm between 2003 and 2015.

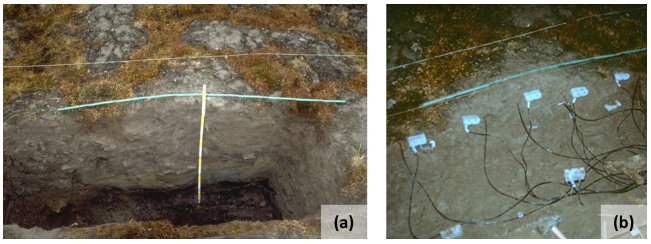

Figure C8. Bayelva soil station, September 1998–January 2012, (78.92094° N, 11.83334° E). **(a)** Soil profile in non-sorted circle (down to 120 cm below ground surface); **(b)** TDR and temperature probes. Soil texture and C, N and S data are listed in Table F1.

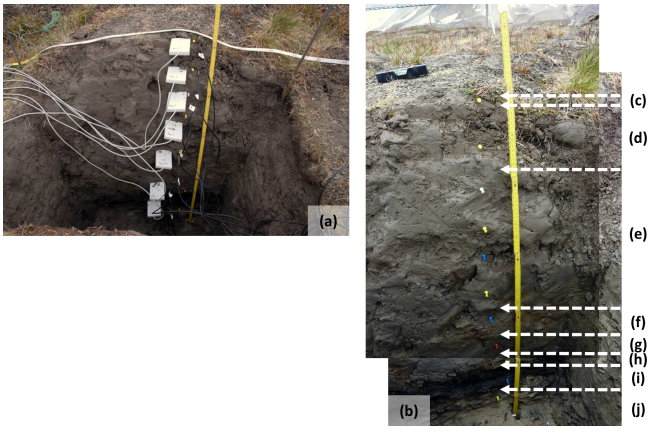

Figure C9. Bayelva soil station, August 2009–present, (78.92094° N, 11.83334° E). **(a)** TDR and temperature probe installation; **(b)** soil characteristics of the non-sorted circle; **(c)** moss layer (0–1 cm), **(d)** loam with roots (1–15 cm), **(e)** loam with few rocks (15–55 cm), **(f)** loam with rocks (55–65 cm), **(g)** dark loam with few rocks (65–77 cm), **(h)** rocky layer with loam (89–95 cm), **(i)** coal layer (81–95 cm), **(j)** rocky layer (95–119 cm). Soil data for texture and C, N and S are listed in Table F1.

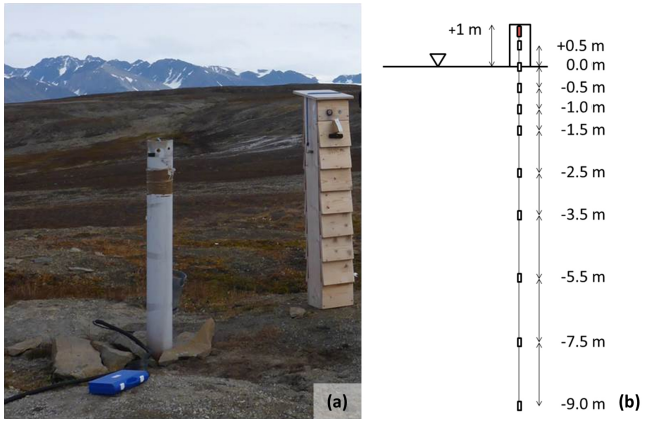

Figure C10. Borehole, Bayelva, drilled in March 2009 (total depth of 9.3 m) and instrumented in August 2009–present, (78.92082° N, 11.83421° E). **(a)** Borehole site with PVC casing outside the borehole and wooden ventilation shield removed. Setup **(b)** with a Geoprecision temperature chain with probes at depths of 0.5 above ground surface and 0, 0.5, 1.0, 1.5, 2.5, 3.5, 5.5, 7.5 and 9 m below ground surface was used for May 2009–September 2015 and May 2016–present.

Appendix D: Calculation and correction of soil and meteorological parameters

D1 Calculation of soil volumetric liquid water content using TDR

The apparent dielectric numbers were converted into liquid water content (θ_l) using the semi-empirical mixing model in Roth et al. (1990). Frozen soil is treated as a four-phase porous medium composed of a solid (soil) matrix and interconnected pore spaces filled with water, ice and air.

The TDR method measures the ratio of apparent to physical probe rod length (L_a/L) which gives the square root of dielectric number (ε_b).

The bulk dielectric number is then calculated from the volumetric fractions and the dielectric numbers of the four phases (details in Appendix A) using

$$\varepsilon_b = \left[\theta_l \varepsilon_l^\alpha + \theta_i \varepsilon_i^\alpha + \theta_s \varepsilon_s^\alpha + \theta_a \varepsilon_a^\alpha\right]^{\frac{1}{\alpha}}. \quad \text{(D1)}$$

A value of 0.5 was used for α.

It is not possible to distinguish between changes in the liquid water content and changes in the ice content with only one measured parameter (ε_b). Equation (D1) was therefore rewritten in terms of the total water content (θ_{tot}) and the porosity (Φ) as

$$\theta_i = \theta_{tot} - \theta_l. \quad \text{(D2)}$$

We remark that Eq. (D2) assumes the densities of liquid and frozen water to be the same. This is clearly wrong for free phases and probably also in the pore space of soils. However, the density ratio can be absorbed into the dielectric number ε_i, which we do in the following. The resulting fluctuation of ε_i is presumed to be small compared to other uncertainties.

$$\theta_s = 1 - \phi \quad \text{(D3)}$$

and

$$\theta_a = \phi - \theta_l - \theta_i = \phi - \theta_{tot} \quad \text{(D4)}$$

to obtain the equation

$$\varepsilon_b = \left[\theta_l \varepsilon_l^\alpha + (\theta_{tot} - \theta_l)\varepsilon_i^\alpha + (1-\phi)\varepsilon_s^\alpha + (\phi - \theta_{tot})\varepsilon_a^\alpha\right]^{\frac{1}{\alpha}}. \quad \text{(D5)}$$

For temperatures above a threshold freezing temperature ($T > T_f$), all water is assumed to be unfrozen (θ_{tot} equals θ_l). Equation (D5) then reduces to

$$\theta_l(T) = \frac{\varepsilon_b^\alpha - \varepsilon_s^\alpha + \phi\left(\varepsilon_s^\alpha - \varepsilon_a^\alpha\right)}{\varepsilon_l^\alpha - \varepsilon_a^\alpha} \text{ if } T > T_f. \quad \text{(D6)}$$

For temperatures equal to or below the threshold freezing temperature ($T \le T_f$) it was assumed that the total water content (θ_{tot}) remained constant and only the ratio between volumetric liquid water content (θ_l) and volumetric ice content (θ_i) changed. This is a rather bold assumption as freezing can lead to high gradients of matric potential, as well as to moisture redistribution. However, since the dielectric number of ice is much smaller than the dielectric number of liquid water, the error in liquid water content measurements is still acceptable (which is not the case for ice content measurements). Under these assumptions we obtained the following equation for calculating the liquid water content of a four-phase mixture:

$$\theta_l(T \le T_f) = \frac{\varepsilon_b^\alpha - \varepsilon_s^\alpha + \phi\left(\varepsilon_s^\alpha - \varepsilon_a^\alpha\right) + \theta_{tot}(\varepsilon_a^\alpha - \varepsilon_i^\alpha)}{\varepsilon_l^\alpha - \varepsilon_i^\alpha}. \quad \text{(D7)}$$

The error of the volumetric water content measurements using TDR probes was estimated to be between 2 and 5 %, and the precision to be better than 0.5 % (Boike and Roth, 1997).

The availability of reliable temperature data is crucial in this approach. The liquid water content is first calculated for all times when the soil temperature was above the freezing threshold, using Eq. (D5). When the soil temperature was below the freezing threshold the water content immediately prior to the onset of freezing was determined and used as total water content (θ_{tot}) for calculating the liquid water content during the frozen interval with Eq. (D7).

Since water in a porous medium does not necessarily freeze at 0 °C but at a temperature that depends on the soil

type and water content, estimating the threshold temperature is a crucial part of this approach. If the freezing characteristic curve is known for the material then the threshold temperature can be determined from the soil liquid water content. To avoid interpretations of frequent freezing and thawing due to soil temperature measurement errors, short-term temperature fluctuations were smoothed by calculating the mean of a moving window with an adjustable width. The smoothed temperatures were then used to trigger the switch from one equation to the other, rather than using the original temperature time series.

D2 Calculation of soil temperatures using raw data and the Steinhart–Hart equation

Temperatures were calculated from the raw voltage data using the Steinhart–Hart equation (Steinhart and Hart, 1968) and sensor calibration at 0 °C (Appendix C). The thermistors were calibrated at 0 °C prior to installation using a deionized water–ice mixture, from which a thermistor-specific offset (δ_o) for the Steinhart–Hart equation was obtained using

$$\frac{1}{T} = 1.28 \times 10^{-3} + 2.37 \times 10^{-4} \times \ln(R_T - \delta_o) + 9.06 \times 10^{-8} \times (\ln(R_T - \delta_o))^3, \quad \text{(D8)}$$

where R_T is the measured resistance and δ_o is the resistance offset at 0 °C. The estimated precision was 2.4×10^{-4} °C at 0 °C with an absolute error of less than 0.1 °C, in the temperature range from −40 to +40 °C.

D3 Correction of net radiation correction for wind speed

D3.1 3 September 1998–18 April 2000

The Campbell Scientific Ltd. Q7 net radiometer was run from 1 September 1998 to 18 April 2000. For positive fluxes ($\mathrm{RadNet_{raw}} > 0\,\mathrm{W\,m^{-2}}$) the correction formula was

$$\mathrm{RadNet} = \mathrm{RadNet_{raw}} \times 1.159 \times \left(1 + \left(\frac{0.066 \times 0.2 \times \mathrm{Vwind}}{0.066 + (0.2 \times \mathrm{Vwind})}\right)\right). \quad \text{(D9)}$$

For negative fluxes ($\mathrm{RadNet_{raw}} < 0\,\mathrm{W\,m^{-2}}$) the correction formula was

$$\mathrm{RadNet} = \mathrm{RadNet_{raw}} \times 0.9065 \times (0.00174 \times \mathrm{Vwind} + 0.99755). \quad \text{(D10)}$$

D3.2 18 April 2000–20 May 2002

The Kipp & Zonen NR Lite net radiometer was run from 18 April 2000 to 20 May 2002. The correction formula was

$$\mathrm{RadNet} = \mathrm{RadNet_{raw}} \times 68.027 \times (1 + (0.0082 \times \mathrm{Vwind})). \quad \text{(D11)}$$

D3.3 20 May 2002–15 September 2003

The Campbell Scientific Ltd. Q7 net radiometer was run from 20 May 2002 to 15 September 2003. For positive fluxes ($\mathrm{RadNet_{raw}} > 0\,\mathrm{W\,m^{-2}}$) the correction formula was

$$\mathrm{RadNet} = \mathrm{RadNet_{raw}} \times 7.71 \times \left(1 + \left(\frac{0.066 \times 0.2 \times \mathrm{Vwind}}{0.066 + (0.2 \times \mathrm{Vwind})}\right)\right). \quad \text{(D12)}$$

For negative fluxes ($\mathrm{RadNet_{raw}} < 0\,\mathrm{W\,m^{-2}}$) the correction formula was

$$\mathrm{RadNet} = \mathrm{RadNet_{raw}} \times 11.66 \times ((0.00174 \times \mathrm{Vwind}) + 0.99755). \quad \text{(D13)}$$

D3.4 15 September 2003–15 August 2009

The Kipp & Zonen NR Lite net radiometer was run from 15 September 2003 to 14 August 2009. The correction formula was

$$\mathrm{RadNet} = \mathrm{RadNet_{raw}} \times 68.0272 \times (1 + (0.0082 \times \mathrm{Vwind})). \quad \text{(D14)}$$

D4 Snow depth correction for air temperature

The raw distance $\mathrm{Dsn_{raw}}$ obtained from the SR50 sonic sensor (Campbell Scientific Ltd.) is calculated using the speed of sound at 0 °C and is corrected with the air temperature at 2 m height using the formula provided by the manufacturer:

$$\mathrm{Dsn} = \mathrm{Dsn_{raw}} \times \sqrt{\frac{T}{273.15}}. \quad \text{(D15)}$$

Appendix E: Description and data of snow profiles

Figure E1. The Bayelva site covered by snow, 7 May 2016.

Figure E2. Snow profile taken on 9 May 2016, inside the Bayelva fenced area. The pockets/holes are the result of snow removal using a snow density cutter (100 cm^3). Snow depth is 47 cm above a basal ice layer at the point of measurement but ranges between 47 and 49 cm. Measurements were taken to the left of the yellow folding rule (left and right profiles in Table E1). Ice layers are present 24–28, 43–47 and 55–56 cm above the basal ice layer, which is 15 cm thick. Further data on temperatures, dielectric numbers and stratigraphy can be found in Table E1.

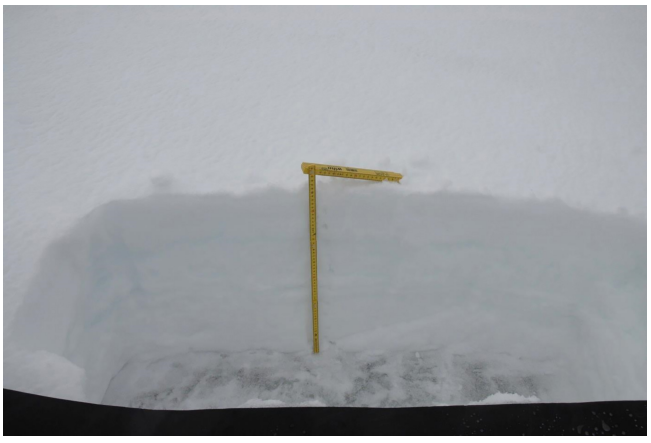

Figure E3. Snow pit, 10 May 2016. The basal ice layer is visible at the bottom of the snow layer. Two profiles were measured: one to the left and one to the right from the yellow meter stick (profile data named left and right in Table E1). Further data on temperatures, dielectric numbers and stratigraphy can be found in Table E1.

Figure E4. Measuring snow temperature in profile, 10 May 2016. Data can be found in Table E1.

Table E1. Snow data obtained from manual probing of snow profiles in spring 2000 (Bayelva), 2006 (Bayelva and Ny-Ålesund) and 2016 (Bayelva). Data include stratigraphy, temperature, dielectric number, density and information on dominant grain shape, size and hand hardness index according to international snow classification (Fierz et al., 2009). Grain shape abbreviations are DH for depth hoar, IFbi for basal ice layer, IFil for horizontal ice layer and PPip for ice pellets. Hand hardness indices are 1 for very soft, 2 for soft, 3 for medium, 4 for hard, 5 for very hard and 6 for ice. Left and right refer to the measurement positions within the profile shown in Fig. E3.

Location	Date*	Air temperature (°C)	Total snow depth (cm)	Min. height above ground surface (cm)	Max. height above ground surface (cm)	Snow temperature (°C)	Dielectric number	Density ($g\,cm^{-3}$)	Grain shape	Grain size (mm)	Hand hardness index (1–6)
Bayelva	2000-04-20		80	0	0	−9.6					
	2000-04-20		80	0	10				DH	3–4	4
	2000-04-20		80	10	10	−10		403			
	2000-04-20		80	10	29					1–3	4
	2000-04-20		80	20	20	−10.9					
	2000-04-20		80	29	52				PPip	2	4
	2000-04-20		80	30	30	−11.4					
	2000-04-20		80	40	40	−12		390			
	2000-04-20		80	50	50	−12.6					
	2000-04-20		80	52	80					< 1	3
	2000-04-20		80	55	55	−13.7					
	2000-04-20		80	60	60	−14.3					
	2000-04-20		80	65	65	−15					
	2000-04-20		80	70	70	−15.5		354			
	2000-04-20		80	75	75	−15.3					
	2000-04-20		80	80	80	−13.6					
Bayelva	2006-05-11		37	0	8				IFbi		6
	2006-05-11		37	8	19					1–2	
	2006-05-11		37	10	10	−1.9					
	2006-05-11		37	13	13	−2.2	3.2				
	2006-05-11		37	18	18	−2.3					
	2006-05-11		37	19	19				IFil		6
	2006-05-11		37	20	27						
	2006-05-11		37	23	23	−2.8	2.2				
	2006-05-11		37	25	25			333			
	2006-05-11		37	27	27		2.1				
	2006-05-11		37	28	28	−4.0					
	2006-05-11		37	33	33	−4.6	2.2				
	2006-05-11		37	37	37	−4.7	2.2				
Ny-Ålesund	2006-05-12	−2.7	30	0	11				IFbi		6
	2006-05-12	−2.7	30	11	24						
	2006-05-12	−2.7	30	12	12	−0.6	2.3				
	2006-05-12	−2.7	30	16	16	−1.4	2.2	304			
	2006-05-12	−2.7	30	21	21	−2.3	2.2				
	2006-05-12	−2.7	30	24	30						
	2006-05-12	−2.7	30	26	26	−3.0	2.2	324			
	2006-05-12	−2.7	30	30	30	−2.7	2.1				
Bayelva	2016-05-09		64	0	15				IFbi		6
(left)	2016-05-09		64	15	15	−2.6					
(left)	2016-05-09		64	18	18		1.3				
(left)	2016-05-09		64	19	19		1.3				
(left)	2016-05-09		64	20	20	−2.2					
(left)	2016-05-09		64	23	27			275			
(left)	2016-05-09		64	24	28				IFil		6
(left)	2016-05-09		64	25	25	−2	1.2				
(left)	2016-05-09		64	30	30	−1.8	1.2				
(left)	2016-05-09		64	35	35	−1.3	1.3				
(left)	2016-05-09		64	37	41			297			
(left)	2016-05-09		64	40	40	−0.9	1.2				
(left)	2016-05-09		64	43	47				IFil		6
(left)	2016-05-09		64	45	45	−0.5	1.2				
(left)	2016-05-09		64	45	49			335			
(left)	2016-05-09		64	50	50	−0.1	1.2				
(left)	2016-05-09		64	53	57			361			
(left)	2016-05-09		64	55	55	0.1	1.3				

Table E1. Continued.

Location	Date*	Air temperature (°C)	Total snow depth (cm)	Min. height above ground surface (cm)	Max. height above ground surface(cm)	Snow temperature (°C)	Dielectric number	Density (g cm^{-3})	Grain shape	Grain size (mm)	Hand hardness index (1–6)
(left)	2016-05-09		64	55	56				IFil		6
(left)	2016-05-09		64	60	60	0.1	1.4				
(left)	2016-05-09		64	60	64			388			
Bayelva	2016-05-09		64	0	15				IFbi		6
(right)	2016-05-09		64	15	15	−2.6					
(right)	2016-05-09		64	20	20	−2.2					
(right)	2016-05-09		64	23	27			294			
(right)	2016-05-09		64	24	28				IFil		6
(right)	2016-05-09		64	25	25	−2	1.3				
(right)	2016-05-09		64	30	30	−1.8	1.2				
(right)	2016-05-09		64	35	35	−1.3	1.3				
(right)	2016-05-09		64	37	41			268			
(right)	2016-05-09		64	40	40	−0.9	1.2				
(right)	2016-05-09		64	43	47				IFil		6
(right)	2016-05-09		64	45	45	−0.5	1.2				
(right)	2016-05-09		64	45	49			319			
(right)	2016-05-09		64	50	50	−0.1	1.5				
(right)	2016-05-09		64	53	57			405			
(right)	2016-05-09		64	55	55	0.1	1.5				
(right)	2016-05-09		64	55	56				IFil		6
(right)	2016-05-09		64	60	60	0.1	1.4				
(right)	2016-05-09		64	60	64			372			
Bayelva	2016-05-10	1	75	0	20				IFbi		6
(left)	2016-05-10	1	75	20	44						3
(left)	2016-05-10	1	75	22	22	−2.5					
(left)	2016-05-10	1	75	24	28			390			
(left)	2016-05-10	1	75	25	25	−2.4	1.3				
(left)	2016-05-10	1	75	28	34			359			
(left)	2016-05-10	1	75	30	30	−2.3	1.3				
(left)	2016-05-10	1	75	30	34			295			
(left)	2016-05-10	1	75	35	35	−1.9	1.3				
(left)	2016-05-10	1	75	38	42			289			
(left)	2016-05-10	1	75	40	40	−1.6	1.3				
(left)	2016-05-10	1	75	40	44				IFil		6
(left)	2016-05-10	1	75	44	50				IFil		6/2
(left)	2016-05-10	1	75	45	45	−1.1					
(left)	2016-05-10	1	75	46	50			400			
(left)	2016-05-10	1	75	48	50				IFil		6
(left)	2016-05-10	1	75	50	50	−0.9	1.3				
(left)	2016-05-10	1	75	50	64						1
(left)	2016-05-10	1	75	52	58			245			
(left)	2016-05-10	1	75	55	55	−0.6	1.3				
(left)	2016-05-10	1	75	58	62			275			
(left)	2016-05-10	1	75	60	60	−0.1	1.2				
(left)	2016-05-10	1	75	62	65				IFil		6
(left)	2016-05-10	1	75	64	68			438			
(left)	2016-05-10	1	75	65	65	0.0	1.4				
(left)	2016-05-10	1	75	65	75						3
(left)	2016-05-10	1	75	68	72			453			
(left)	2016-05-10	1	75	70	70	0.1	1.5				
(left)	2016-05-10	1	75	72	72		1.4				
(left)	2016-05-10	1	75	72	76			414			
(left)	2016-05-10	1	75	73	73		1.4				
(left)	2016-05-10	1	75	74	74		1.4				
(left)	2016-05-10	1	75	75	75	0.1					
Bayelva	2016-05-10	1	75	0	20				IFbi		6
(right)	2016-05-10	1	75	20	44						3
(right)	2016-05-10	1	75	22	22	−2.5					
(right)	2016-05-10	1	75	23	23		1.4				
(right)	2016-05-10	1	75	24	28			340			

Table E1. Continued.

Location	Date*	Air temperature (°C)	Total snow depth (cm)	Min. height above ground surface (cm)	Max. height above ground surface(cm)	Snow temperature (°C)	Dielectric number	Density (g cm^{-3})	Grain shape	Grain size (mm)	Hand hardness index (1–6)
(right)	2016-05-10	1	75	25	25	−2.4					
(right)	2016-05-10	1	75	28	34			357			
(right)	2016-05-10	1	75	30	30	−2.3	1.3				
(right)	2016-05-10	1	75	30	34			362			
(right)	2016-05-10	1	75	35	35	−1.9	1.3				
(right)	2016-05-10	1	75	38	42			290			
(right)	2016-05-10	1	75	40	40	−1.6	1.2				
(right)	2016-05-10	1	75	40	44				IFil		6
(right)	2016-05-10	1	75	44	50				IFil		6/2
(right)	2016-05-10	1	75	45	45	−1.1	1.3				
(right)	2016-05-10	1	75	46	50			393			
(right)	2016-05-10	1	75	48	50				IFil		6
(right)	2016-05-10	1	75	50	50	−0.9	1.2				
(right)	2016-05-10	1	75	50	64						1
(right)	2016-05-10	1	75	52	58			244			
(right)	2016-05-10	1	75	55	55	−0.6	1.2				
(right)	2016-05-10	1	75	58	62			316			
(right)	2016-05-10	1	75	60	60	−0.1	1.2				
(right)	2016-05-10	1	75	62	65				IFil		6
(right)	2016-05-10	1	75	64	68			395			
(right)	2016-05-10	1	75	65	65	0.0	1.3				
(right)	2016-05-10	1	75	65	75						3
(right)	2016-05-10	1	75	68	72			421			
(right)	2016-05-10	1	75	70	70	0.1	1.4				
(right)	2016-05-10	1	75	72	72						
(right)	2016-05-10	1	75	72	76			392			
(right)	2016-05-10	1	75	73	73		1.4				
(right)	2016-05-10	1	75	74	74						
(right)	2016-05-10	1	75	75	75	0.1					

* YYYY-MM-DD

Appendix F: Description and data of soil profiles

Table F1. Soil data from the soil pits in 1998, 2007 and 2009. The location of the soil profiles (including pictures and location) is given in Appendix C and Fig. 2a. Grain size class according to Folk (1954): S, sand; s, sandy; Z, silt; z, silty; M, mud; m, muddy; C, clay; c, clayey. In 2009 at depths of 30 and 35 cm, high total organic content (TOC), soil organic carbon content (SOCC), bulk carbon density (CD_{bulk}) and carbon (C) values possible due to natural coal in the soil profile.

Coordinates (Lat, long)	Date (YYYY)	Cross section/ profile	Depth below surface (cm)	Layer thickness (cm)	TOC (wt %)	SOCC ($kg\,m^{-2}$)	CD_{bulk} ($kg\,m^{-3}$)	C (wt %)	N (wt %)	S (wt %)	Dry bulk density ($g\,cm^{-3}$)	Average dry bulk density ($g\,cm^{-3}$)	Grain size class
78.92094° N, 11.83334° E	1998	Figs. C7a and C8	11	11	1.3	2.5	22.8	1.3	< 0.1	< 0.05		1.7	sZ
78.92094° N, 11.83334° E	1998	Figs. C7a and C8	35	24	1.1	4.5	18.7	1.1	< 0.1	< 0.05		1.7	sM
78.92094° N, 11.83334° E	1998	Figs. C7a and C8	50	15	0.7	1.8		0.8	< 0.1	< 0.05		1.7	
78.92094° N, 11.83334° E	1998	Figs. C7a and C8	61	11	3.0	5.6	50.5	2.8	< 0.1	< 0.05		1.7	M
78.92094° N, 11.83334° E	1998	Figs. C7a and C8	69	8	21.2	28.9		23.8	0.4	0.4		1.7	
78.92094° N, 11.83334° E	1998	Figs. C7a and C8	80	11	4.4	8.2		4.3	0.1	0.3		1.7	
78.92094° N, 11.83334° E	1998	Figs. C7a and C8	6	6	1.1	1.1	18.2	1.2	< 0.1	< 0.05		1.7	sZ
78.92094° N, 11.83334° E	1998	Figs. C7a and C8	31	25	1.4	5.7	23.0	1.3	< 0.1	< 0.05		1.7	sZ
78.92094° N, 11.83334° E	1998	Figs. C7a and C8	51	20	1.2	4.2	20.9	1.2	< 0.1	< 0.05		1.7	sM
78.92094° N, 11.83334° E	1998	Figs. C7a and C8	63	12	1.1	2.2	18.2	1.1	< 0.1	< 0.05		1.7	M
78.92094° N, 11.83334° E	1998	Figs. C7a and C8	72	9	2.9	4.4	48.6	2.8	0.1	0.1		1.7	M
78.92094° N, 11.83334° E	1998	Figs. C7a and C8	80	8	29.4	40.0		34.3	0.6	0.6		1.7	
78.92094° N, 11.83334° E	1998	Figs. C7a and C8	82	2	4.1	1.4		4.1	0.1	0.1		1.7	
78.92094° N, 11.83334° E	1998	Figs. C7a and C8	86	4	3.8	2.6	63.9	3.7	0.1	0.2		1.7	C
78.92094° N, 11.83334° E	1998	Figs. C7a and C8	10	10	0.7	1.2	12.2	0.8	< 0.1	< 0.05		1.7	sM
78.92094° N, 11.83334° E	1998	Figs. C7a and C8	39	29	0.6	3.1	10.5	0.7	< 0.1	< 0.05		1.7	M
78.92094° N, 11.83334° E	1998	Figs. C7a and C8	70	31	1.0	5.5		1.1	< 0.1	< 0.05		1.7	
78.92094° N, 11.83334° E	1998	Figs. C7a and C8	75	5	2.7	2.3	46.4	2.7	< 0.1	< 0.05		1.7	M
78.92094° N, 11.83334° E	1998	Figs. C7a and C8	80	5	5.1	4.3	85.9	6.6	0.2	0.2		1.7	C
78.92094° N, 11.83334° E	1998	Figs. C7a and C8	91	11	6.5	12.1	110.0	6.4	0.2	0.5		1.7	C
78.92094° N, 11.83334° E	1998	Figs. C7a and C8	10	10	1.3	2.2	21.8	1.3	< 0.1	< 0.05		1.7	sM
78.92094° N, 11.83334° E	1998	Figs. C7a and C8	33	23	1.0	4.1	17.7	1.0	< 0.1	< 0.05		1.7	M
78.92094° N, 11.83334° E	1998	Figs. C7a and C8	57	24	0.8	3.1	12.9	0.8	< 0.1	< 0.05		1.7	M
78.92094° N, 11.83334° E	1998	Figs. C7a and C8	69	12	0.7	1.3	11.2	0.8	< 0.1	< 0.05		1.7	M
78.92094° N, 11.83334° E	1998	Figs. C7a and C8	82	13	3.0	6.6	51.0	2.9	0.1	0.1		1.7	M
78.92094° N, 11.83334° E	1998	Figs. C7a and C8	88	6	3.7	3.7	62.1	3.4	0.1	0.1		1.7	M
78.92094° N, 11.83334° E	1998	Figs. C7a and C8	11	11	2.0	3.8	34.3	2.0	0.1	< 0.05		1.7	sZ
78.92094° N, 11.83334° E	1998	Figs. C7a and C8	25	14	1.2	2.8	19.7	1.0	< 0.1	< 0.05		1.7	sM
78.92094° N, 11.83334° E	1998	Figs. C7a and C8	50	25	1.2	5.0	19.9	1.1	< 0.1	< 0.05		1.7	M
78.92094° N, 11.83334° E	1998	Figs. C7a and C8	60	12	1.2	2.4		1.2	< 0.1	< 0.05		1.7	
78.92094° N, 11.83334° E	1998	Figs. C7a and C8	70	8	1.3	1.8	21.9	1.8	< 0.1	< 0.05		1.7	M
78.92094° N, 11.83334° E	1998	Figs. C7a and C8	83	13	3.3	7.3	56.3	3.7	< 0.1	0.1		1.7	sM

The soil organic carbon content ($kg\,m^{-2}$) has been calculated using the following formula:

$$SOCC = TOC \times \overline{\rho}_{bulk} \times z = CD_{bulk} \times z. \quad (F1)$$

The bulk carbon density (CD_{bulk}) ($kg\,m^{-3}$) has been calculated using the bulk soil density ρ_{bulk} and the following formula:

$$CD_{bulk} = TOC \times \overline{\rho}_{bulk} = \frac{SOCC}{z}. \quad (F2)$$

Table F1. Continued.

Coordinates (Lat, long)	Date (YYYY)	Cross section/ profile	Depth below surface (cm)	Layer thickness (cm)	TOC (wt %)	SOCC ($kg\,m^{-2}$)	CD_b ($kg\,m^{-3}$)	C (wt %)	N (wt %)	S (wt %)	Dry bulk density ($g\,cm^{-3}$)	Average dry bulk density ($g\,cm^{-3}$)	Grain size class
78.92085° N, 11.83182° E	2007	Fig. 2a	0	0				1.3	< 0.1	< 0.05	0.8	1.5	sZ
78.92085° N, 11.83182° E	2007	Fig. 2a	15	15	1.1	2.8	18.6				1.7	1.5	
78.92085° N, 11.83182° E	2007	Fig. 2a	30	15	0.7	1.9	12.8				1.8	1.5	
78.92085° N, 11.83182° E	2007	Fig. 2a	45	15	2.2	5.1	33.9				1.5	1.5	
78.92085° N, 11.83182° E	2007	Fig. 2a	60	15	0.8	2.0	13.6				1.7	1.5	
78.92091° N, 11.84445° E	2007	Fig. 2a	15	15				2.8	< 0.1	< 0.05	1.8	1.7	sZ
78.92091° N, 11.84445° E	2007	Fig. 2a	30	15	1.5	3.5	23.6				1.6	1.7	
78.92091° N, 11.84445° E	2007	Fig. 2a	45	15	1.4	3.4	22.7				1.6	1.7	
78.92091° N, 11.84445° E	2007	Fig. 2a	60	15				2.3	< 0.1	< 0.05	1.7	1.7	sZ
78.92091° N, 11.84445° E	2007	Fig. 2a	70	10	1.2	1.9	19.1				1.6	1.7	
78.92091° N, 11.84445° E	2007	Fig. 2a	82	12	1.2	2.7	22.1				1.8	1.7	
78.92091° N, 11.84445° E	2007	Fig. 2a	95	13				2.9	< 0.1	< 0.05	1.7	1.7	sZ
78.92091° N, 11.84445° E	2007	Fig. 2a	105	10	1.3	2.2	21.8				1.7	1.7	
78.92091° N, 11.84445° E	2007	Fig. 2a	110	5				2.4	< 0.1	< 0.05	1.6	1.7	sZ
78.92197° N, 11.84503° E	2007	Fig. 2a	15	15				2.0	0.1	< 0.05	1.4	1.5	sZ
78.92197° N, 11.84503° E	2007	Fig. 2a	30	15	1.1	2.2	15.0				1.4	1.5	
78.92197° N, 11.84503° E	2007	Fig. 2a	40	10	1.7	2.4	23.6				1.4	1.5	
78.92197° N, 11.84503° E	2007	Fig. 2a	50	10	1.0	1.5	15.3	2.0	< 0.1	< 0.05	1.5	1.5	sZ
78.92197° N, 11.84503° E	2007	Fig. 2a	65	15				1.5	< 0.1	0.1	1.4	1.5	sZ
78.92197° N, 11.84503° E	2007	Fig. 2a	80	15	0.5	1.1	7.6				1.5	1.5	
78.92197° N, 11.84503° E	2007	Fig. 2a	100	20	0.9	2.8	14.0				1.6	1.5	
78.92197° N, 11.84503° E	2007	Fig. 2a	125	25				0.9	< 0.1	< 0.05	1.8	1.5	sZ
78.92094° N, 11.83334° E	2009	Figs. C7c and C9	5	5							2.1	2.2	
78.92094° N, 11.83334° E	2009	Figs. C7c and C9	19	19	1.3	5.6	29.5	1.8	< 0.1	0.3	2.2	2.2	sZ
78.92094° N, 11.83334° E	2009	Figs. C7c and C9	30	11	15.7	37.7	345.8	15.4	0.4	1.0		2.2	zS
78.92094° N, 11.83334° E	2009	Figs. C7c and C9	35	5	51.2	55.9	1126.7	45.7	1.1	1.9	2.2	2.2	Z
78.92094° N, 11.83334° E	2009	Figs. C7c and C9	50	15	2.2	7.4	49.5	2.4	0.1	0.2		2.2	sZ
78.92094° N, 11.83334° E	2009	Figs. C7c and C9	60	10	1.5	3.3	33.3	1.8	< 0.1	0.2		2.2	sZ
78.92094° N, 11.83334° E	2009	Figs. C7c and C9	70	10	0.8	1.7	17.3	1.0	< 0.1	0.2		2.2	sZ
78.92094° N, 11.83334° E	2009	Figs. C7c and C9	80	10	1.5	3.3	33.5	1.7	0.1	0.2		2.2	sZ
78.92094° N, 11.83334° E	2009	Figs. C7c and C9	90	10	1.0	2.3	22.8	1.2	< 0.1	0.2		2.2	sZ
78.92094° N, 11.83334° E	2009	Figs. C7c and C9	100	10	0.9	1.9	19.4	1.0	< 0.1	0.2		2.2	sZ
78.92094° N, 11.83334° E	2009	Figs. C7c and C9	110	10	0.9	2.1	20.7	1.1	< 0.1	0.2		2.2	sZ
78.92094° N, 11.83334° E	2009	Figs. C7c and C9	120	10	1.1	2.3	23.5	1.2	< 0.1	0.2		2.2	sZ

Appendix G: Names of the variables and units for data files

Table G1. Overview of all variables provided as time series. The variables electric conductivity, dielectric number, soil temperature and volumetric soil liquid water content include a second number or letter in the column name. In these cases, the first number is the distance in the 2-D profile and the second is the depth. The single letters (a, b, c, d) refer to the different 1-D profiles. Vertically oriented probes are marked with letter (v). Additional level 2 data are provided for the variables snow depth, soil temperature and volumetric soil liquid water content, which is indicated by "_lv2" in the column names. If an air temperature sensor is covered by snow and thus measures snow temperature, this is indicated by a flag in the data.

Variable	Column name	Unit
Air–snow temperature	Tair_(height in cm)	°C
Relative humidity	RH_(height in cm)	%
Incoming shortwave radiation	SwIn	$W\,m^{-2}$
Outgoing shortwave radiation	SwOut	$W\,m^{-2}$
Incoming longwave radiation	LwIn	$W\,m^{-2}$
Outgoing longwave radiation	LwOut	$W\,m^{-2}$
Net radiation	RadNet	$W\,m^{-2}$
Wind speed	Vwind_(height in cm)	$m\,s^{-1}$
Wind direction	Dirwind_(height in cm)	°
Wind direction standard deviation	Dirwind_sd_(height in cm)	°
Soil and permafrost temperature	Ts_(depth in cm)	°C
Soil bulk electrical conductivity	Cond_(depth in cm)	$S\,m^{-1}$
Dielectric number	E2_(depth in cm)	–
Soil volumetric liquid water content	Vwc_(depth in cm)	–
Ground heat flux	G	$W\,m^{-2}$
Precipitation (liquid)	Prec	mm
Snow depth	Dsn	m

Appendix H: Time series plots

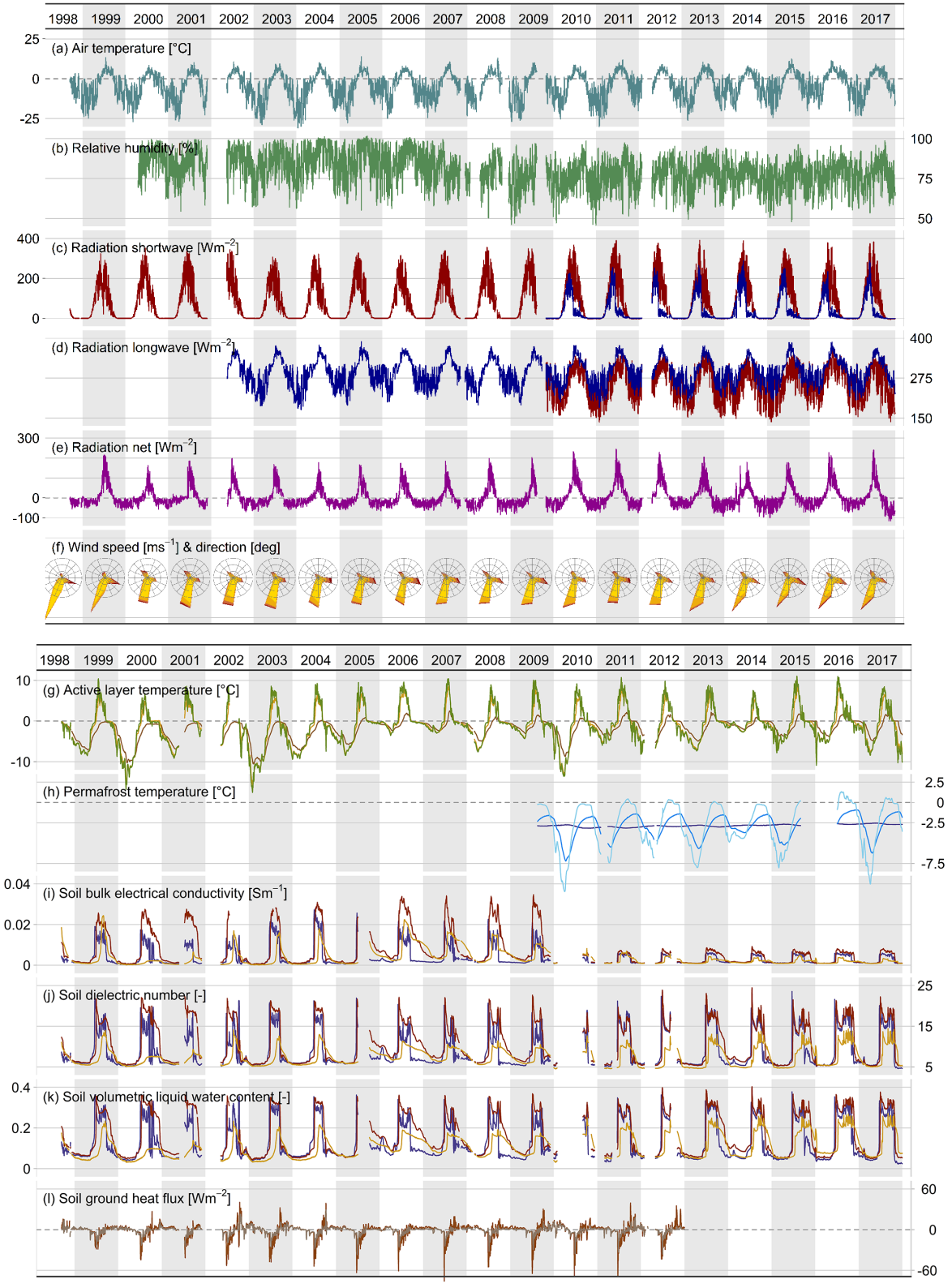

Figure H1.

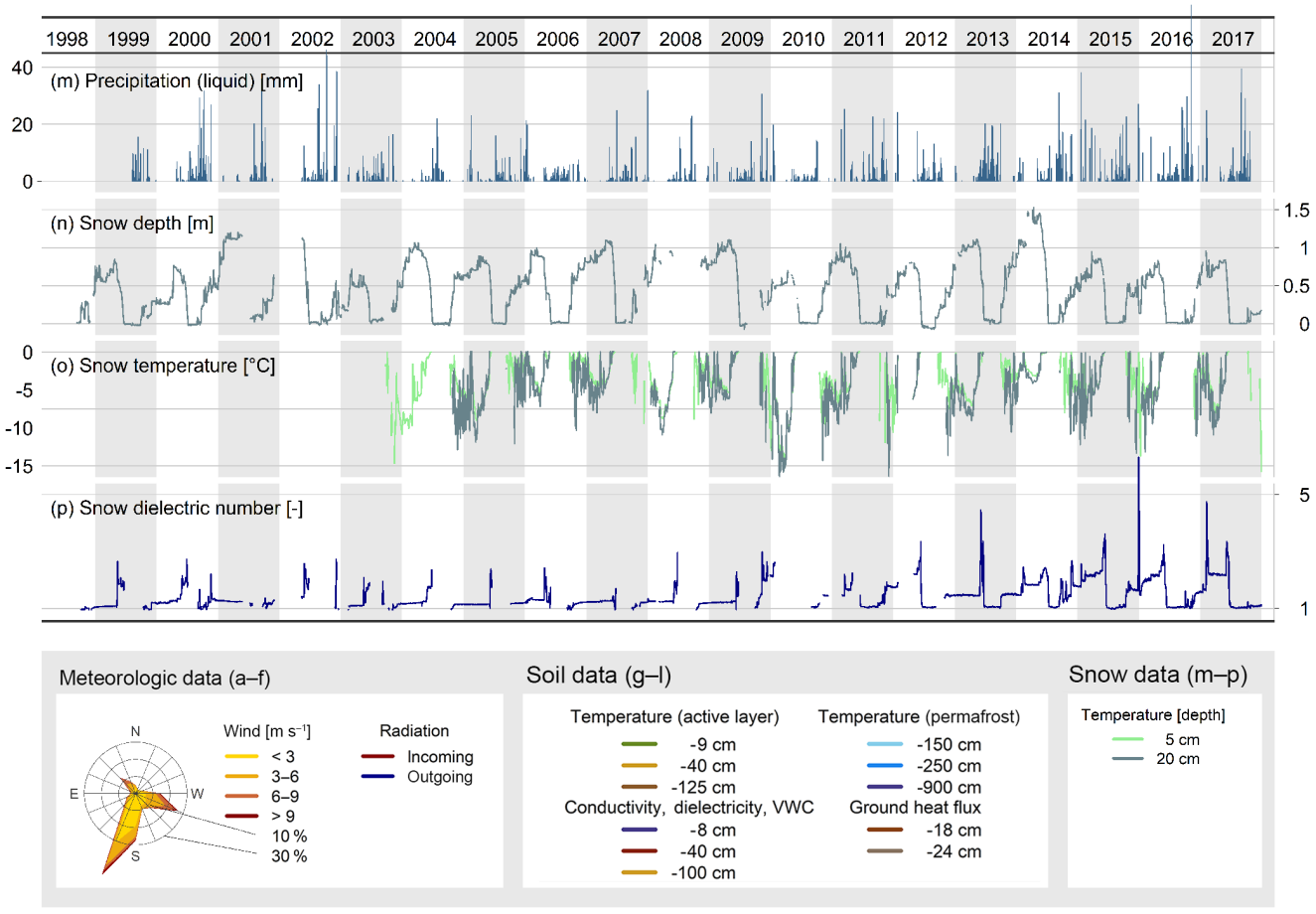

Figure H1. Time series of Bayelva data provided in this paper (Fig. 3) divided into three plots. **(a–f)** Meteorological data; **(g–l)** soil and subsurface data; **(m–p)** snow data. The data are organized following the structure of Appendix G. Further details on the sensors and periods of operation are given in Table 2.

The Supplement related to this article is available online at https://doi.org/10.5194/essd-10-355-2018-supplement.

Competing interests. The authors declare that they have no conflict of interest.

Special issue statement. This article is part of the special issue "Changing Permafrost in the Arctic and its Global Effects in the 21st Century (PAGE21) (BG/ESSD/GMD/TC inter-journal SI)". It is not associated with a conference.

Acknowledgements. The logistical support provided by the AWIPEV research base at Ny-Ålesund is gratefully acknowledged. Field support, including data collection, was also provided by Konstanze Piel, Christian Wille, Steffen Frey, Conrad Kopsch, Günther Stoof and Peter Schreiber. We appreciate the support of Klaus-Dieter Matz and Frank Scholten for the preparation of the GeoTIFF versions of the HRSC-AX data products. The authors acknowledge the financial support provided through the European Union's FP7-ENV PAGE21 project under contract number GA282700. We thank the two anonymous reviewers whose comments helped to improve this paper.

The article processing charges for this open-access publication were covered by a Research Centre of the Helmholtz Association.

Edited by: David Carlson
Reviewed by: two anonymous referees

References

Beringer, J., Lynch, A. H., Chapin, F. S., Mack, M., and Bonan, G.: The Representation of Arctic Soils in the Land Surface Model: The Importance of Mosses, J. Climate, 14, 3324–3335, 2001.

Boike, J. and Roth, K.: Time Domain Reflectometry as a Field Method for Measuring Water Content and Soil Water Electrical Conductivity at a Continuous Permafrost Site, Permafrost Periglac., 8, 359–370, 1997.

Boike, J., Hinzman, L. D., Overduin, P. P., Romanovsky, V., Ippisch, O., and Roth, K.: A Comparison of Snow Melt at Three Circumpolar Sites: Spitsbergen, Siberia, Alaska, in: Proceedings of the 8th International Conference on Permafrost, Zuerich, Switzerland, 20–25 July 2003, 2003a.

Boike, J., Roth, K., and Ippisch, O.: Seasonal Snow Cover on Frozen Ground: Energy Balance Calculations of a Permafrost Site Near Ny-Ålesund, Spitsbergen, J. Geophys. Res., 108, 8163, https://doi.org/10.1029/2001JD000939, 2003b.

Boike, J., Ippisch, O., Overduin, P. P., Hagedorn, B., and Roth, K.: Water, heat and solute dynamics of a mud boil, Spitsbergen, Geomorphology, 95, 61–73, 2008a.

Boike, J., Wille, C., and Abnizova, A.: Climatology and summer energy and water balance of polygonal tundra in the Lena River Delta, Siberia, J. Geophys. Res., 113, G03025, https://doi.org/10.1029/2007JG000540, 2008b.

Boike, J., Langer, M., Lantuit, H., Muster, S., Roth, K., Sachs, T., Overduin, P., Westermann, S., and McGuire, A. D.: Permafrost – Physical Aspects, Carbon Cycling, Databases and Uncertainties, in: Recarbonization of the Biosphere: Ecosystems and the Global Carbon Cycle, edited by: Lal, R., Springer Science + Business Media, 2012.

Brattbakk, I.: Ny-Ålesund, Brøggerhalvøya, Svalbard, K. Norske Vidensk. Selsk. Mus. Bot. avd. Trondheim, Norsk Polarinstitutt, Oslo, Vegetasjonskart, 1981.

Brown, J., Ferrians Jr, O. J., Heginbottom, J., and Melnikov, E.: Circum-Arctic map of permafrost and ground-ice conditions, National Snow and Ice Data Center/World Data Center for Glaciology, Boulder, CO, 1998.

Cannone, N., Guglielmin, M., and Gerdol, R.: Relationships between vegetation patterns and periglacial landforms in northwestern Svalbard, Polar Biol., 27, 562–571, 2004.

Cannone, N., Augusti, A., Malfasi, F., Pallozzi, E., Calfapietra, C., and Brugnoli, E.: The interaction of biotic and abiotic factors at multiple spatial scales affects the variability of CO_2 fluxes in polar environments, Polar Biol., 39, 1581–1596, 2016.

CAVM-Team: Circumpolar Arctic Vegetation Map. (1 : 7 500 000 scale), US Fish and Wildlife Service, Anchorage, USA, 2005.

Chadburn, S. E., Krinner, G., Porada, P., Bartsch, A., Beer, C., Belelli Marchesini, L., Boike, J., Ekici, A., Elberling, B., Friborg, T., Hugelius, G., Johansson, M., Kuhry, P., Kutzbach, L., Langer, M., Lund, M., Parmentier, F.-J. W., Peng, S., Van Huissteden, K., Wang, T., Westermann, S., Zhu, D., and Burke, E. J.: Carbon stocks and fluxes in the high latitudes: using site-level data to evaluate Earth system models, Biogeosciences, 14, 5143–5169, https://doi.org/10.5194/bg-14-5143-2017, 2017.

Christiansen, H. H., Etzelmüller, B., Isaksen, K., Juliussen, H., Farbrot, H., Humlum, O., Johansson, M., Ingeman Nielsen, T., Kristensen, L., Hjort, J., Holmlund, P., Sannel, A. B. K., Sigsgaard, C., Aakerman, J. H., Foged, N., Blikra, L. H., Pernosky, M. A., and Odegard, R.: The thermal state of permafrost in the nordic area during the international polar year 2007–2009, Permafrost Periglac., 21, 156–181, 2010.

Ekici, A., Beer, C., Hagemann, S., Boike, J., Langer, M., and Hauck, C.: Simulating high-latitude permafrost regions by the JSBACH terrestrial ecosystem model, Geosci. Model Dev., 7, 631–647, https://doi.org/10.5194/gmd-7-631-2014, 2014.

Ekici, A., Chadburn, S., Chaudhary, N., Hajdu, L. H., Marmy, A., Peng, S., Boike, J., Burke, E., Friend, A. D., Hauck, C., Krinner, G., Langer, M., Miller, P. A., and Beer, C.: Site-level model intercomparison of high latitude and high altitude soil thermal dynamics in tundra and barren landscapes, The Cryosphere, 9, 1343–1361, https://doi.org/10.5194/tc-9-1343-2015, 2015.

Fierz, C., Armstrong, R. L., Durand, Y., Etchevers, P., Greene, E., McClung, D. M., Nishimura, K., Satyawali, P. K., and Sokratov, S. A.: The international classification for seasonal snow on the ground, IHP-VII Technical Documents in Hydrology No. 83, IACS Contribution No. 1, UNESCO-IHP, Paris, 2009.

Folk, R. L.: The distinction between grain size and mineral composition in sedimentary-rock nomenclature, J. Geology, 62, 344–359, 1954.

Førland, E. J., Benestad, R., Hanssen-Bauer, I., Haugen, J. E., and Skaugen, T. E.: Temperature and Precipitation Develop-

ment at Svalbard 1900–2100, Adv. Meteorology, 2011, 893790, https://doi.org/10.1155/2011/893790, 2011.

Gwinner, K., Hauber, E., Hoffmann, H., Scholten, F., Jaumann, R., Neukum, G., Coltelli, M., and Puglisi, G.: The HRSC-A experiment on high resolution imaging and DEM generation at the Aeolian Islands, Proceedings of the 13th International Conference on Applied Geologic Remote Sensing, Ann Arbor, Michigan, USA, 560–569, 1999.

Gwinner, K., Hauber, E., Jaumann, R., and Neukum, G.: High-resolution, digital photogrammetric mapping: A tool for Earth science, EOS T. Am. Geophys. Un., 81, 513–520, 2000.

Gwinner, K., Scholten, F., Spiegel, M., Schmidt, R., Giese, B., Oberst, J., Jaumann, R., Neukum, G., and Team, H. C.-I.: Hochauflösende Digitale Geländemodelle auf der Grundlage von Mars Express HRSC-Daten, Photogramm. Fernerkun., 5, 387–394, 2005.

Gwinner, K., Scholten, F., Preusker, F., Elgner, S., Roatsch, T., Spiegel, M., Schmidt, R., Oberst, J., Jaumann, R., and Heipke, C.: Topography of Mars from global mapping by HRSC high-resolution digital elevation models and orthoimages: Characteristics and performance, Earth Planet. Sci. Lett., 294, 506–519, https://doi.org/10.1016/j.epsl.2009.11.007, 2010.

Gwinner, K., Coltelli, M., Flohrer, J., Jaumann, R., Matz, K.-D., Marsella, M., Roatsch, T., Scholten, F., and Trauthan, F.: The HRSC-AX MT. ETNA project: High-resolution orthoimages and 1 m dem at regional scale, Int. Arch. Photogramm., XXXVI Part 1, 6 pp., 2006.

Gwinner, K., Jaumann, R., Hauber, E., Hoffmann, H., Heipke, C., Oberst, J., Neukum, G., Ansan, V., Bostelmann, J., Dumke, A., Elgner, S., Erkeling, G., Fueten, F., Hiesinger, H., Hoekzema, N. M., Kersten, E., Loizeau, D., Matz, K.-D., McGuire, P. C., Mertens, V., Michael, G., Pasewaldt, A., Pinet, P., Preusker, F., Reiss, D., Roatsch, T., Schmidt, R., Scholten, F., Spiegel, M., Stesky, R., Tirsch, D., van Gasselt, S., Walter, S., Wählisch, M., and Willner, K.: The High Resolution Stereo Camera (HRSC) of Mars Express and its approach to science analysis and mapping for Mars and its satellites, Plan. Space Sci., 126, 93–138, 2016.

Hanssen-Bauer, I. and Førland, E. J.: Long-Term Trends in Precipitation and Temperature in the Norwegian Arctic: Can They be Explained by Changes in Atmospheric Circulation Patterns, Clim. Res., 10, 143–153, 1998.

Hauber, E., Reiss, D., Ulrich, M., Preusker, F., Trauthan, F., Zanetti, M., Hiesinger, H., Jaumann, R., Johansson, L., and Johnsson, A.: Landscape evolution in Martian mid-latitude regions: insights from analogous periglacial landforms in Svalbard, Geological Society, London, Special Publications, 356, 111–131, https://doi.org/10.1144/SP356.7, 2011a.

Hauber, E., Reiss, D., Ulrich, M., Preusker, F., Trauthan, F., Zanetti, M., Hiesinger, H., Jaumann, R., Johansson, L., Johnsson, A., Olvmo, M., Carlsson, E., Johansson, H. A. B., and McDaniel, S.: Periglacial landscapes on Svalbard: Terrestrial analogs for cold-climate landforms on Mars, Geol. S. Am. S., 483, 177–201, 2011b.

Heimovaara, T. J. and de Water, E.: A Computer Controlled TDR System for Measuring Water Content and Bulk Electrical Conductivity, Laboratory of Physical Geography and Soil Science, University of Amsterdam, Amsterdam, 1993.

Heimovaara, T. J., Focke, A. G., Bouten, W., and Verstraten, J. M.: Assessing Temporal Variations in Soil Water Composition With Time Domain Reflectometry, Soil Sci. Soc. Am. J., 59, 689–698, 1995.

Hjelle, A., Piepjohn, K., Saalmann, K., Ohta, Y., Salvigsen, O., Thiedig, F., and Dallmann, W. K.: A7G Kongsfjorden 1 : 100 000, mapped by: Midbøe, P. S., Ohta, Y., Manby, G. M., Thiedig, F., Saalmann, K., Sidow, H., Ludwig, P., Weber, A., Hincke, A., and von Wuthenau, K., 1980s, final compilation by: Hjelle, A., Ohta, Y., and Piepjohn, K., 1998, Norwegian Polar Institute (NPI), 1999.

Hodson, A., Tranter, M., Gurnell, A., Clark, M., and Hagen, J. O.: The hydrochemistry of Bayelva, a high arctic proglacial stream in Svalbard, J. Hydrol., 257, 91–114, 2002.

Humlum, O.: Holocene permafrost aggradation in Svalbard, Geol. Soc. Spec. Publ., 242, 119–129, 2005.

Ippisch, O.: Coupled Transport in Natural Porous Media, Doctor of Natural Sciences, Rupertus Carola University of Heidelberg, Germany, 144 pp., 2001.

Isaksen, K., Holmlund, P., Sollid, J. L., and Harris, C.: Three Deep Alpine-Permafrost Boreholes in Svalbard and Scandinavia, Permafrost Periglac., 12, 13–25, 2001.

Isaksen, K., Benestad, R. E., Harris, C., and Sollid, J. L.: Recent extreme near-surface permafrost temperatures on Svalbard in relation to future climate scenarios, Geophys. Res. Lett., 34, L17502, https://doi.org/10.1029/2007GL031002, 2007a.

Isaksen, K., Sollid, J. L., Holmlund, P., and Harris, C.: Recent warming of mountain permafrost in Svalbard and Scandinavia, J. Geophys. Res.-Earth, 112, F02S04, https://doi.org/10.1029/2006JF000522, 2007b.

Koven, C. D., Riley, W. J., and Stern, A.: Analysis of permafrost thermal dynamics and response to climate change in the CMIP5 Earth System Models, J. Climate, 26, 1877–1900, 2012.

Langer, M., Westermann, S., Heikenfeld, M., Dorn, W., and Boike, J.: Satellite-based modeling of permafrost temperatures in a tundra lowland landscape, Remote Sens. Environ., 135, 12–24, 2013.

Lloyd, C. R.: The measurement and modelling of the carbon dioxide exchange at a high Arctic site in Svalbard, Glob. Change Biol., 7, 405–426, 2001a.

Lloyd, C. R.: On the Physical Controls of the Carbon Dioxide Balance at a High Arctic Site in Svalbard, Theor. Appl. Climatol., 70, 167–182, 2001b.

Lloyd, C. R., Harding, R. J., Friborg, T., and Aurela, M.: Surface Fluxes of Heat and Water Vapour from Sites in the European Arctic, Theor. Appl. Climatol., 70, 19–33, 2001.

López-Moreno, J. I., Boike, J., Sanchez-Lorenzo, A., and Pomeroy, J. W.: Impact of climate warming on snow processes in Ny-Ålesund, a polar maritime site at Svalbard, Global Planet. Change, 146, 10–21, 2016.

Lüers, J. and Boike, J.: Time series of annual atmospheric CO_2-fluxes above a high-arctic permafrost site, Svalbard (Norway), 2008-03 to 2009-03, Department of Micrometeorology, University of Bayreuth, 2013.

Lüers, J., Westermann, S., Piel, K., and Boike, J.: Annual CO_2 budget and seasonal CO_2 exchange signals at a high Arctic permafrost site on Spitsbergen, Svalbard archipelago, Biogeosciences, 11, 6307–6322, https://doi.org/10.5194/bg-11-6307-2014, 2014.

Maturilli, M. and Kayser, M.: Arctic warming, moisture increase and circulation changes observed in the Ny-Ålesund homog-

enized radiosonde record, Theor. Appl. Climatol., 130, 1–17, https://doi.org/10.1007/s00704-016-1864-0, 2016.

Maturilli, M., Herber, A., and König-Langlo, G.: Climatology and time series of surface meteorology in Ny-Ålesund, Svalbard, Earth Syst. Sci. Data, 5, 155–163, https://doi.org/10.5194/essd-5-155-2013, 2013.

Maturilli, M., Herber, A., and König-Langlo, G.: Surface radiation climatology for Ny-Ålesund, Svalbard (78.9° N), basic observations for trend detection, Theor. Appl. Climatol., 120, 331–339, 2014.

Muraoka, H., Noda, H., Uchida, M., Ohtsuka, T., Koizumi, H., and Nakatsubo, T.: Photosynthetic characteristics and biomass distribution of the dominant vascular plant species in a high Arctic tundra ecosystem, Ny-Ålesund, Svalbard: implications for their role in ecosystem carbon gain, J. Plant Res., 121, 137–145, 2008.

Ohtsuka, T., Adachi, M., Uchida, M., and Nakatsubo, T.: Relationships between vegetation types and soil properties along a topographical gradient on the northern coast of the Brøgger Peninsula, Svalbard, Polar Biosci., 19, 63–72, 2006.

Overduin, P. P. and Kane, D. L.: Frost Boils and Soil Ice Content: Field Observations, Permafrost Periglac., 17, 291–307, 2006.

Romanovsky, V., Isaksen, K., Drozdov, D., Anisimov, O., Instanes, A., Leibman, M., McGuire, A. D., Shiklomanov, N., Smith, S., and Walker, D.: Changing permafrost and its impacts, in: Snow, Water, Ice and Permafrost in the Arctic (SWIPA) 2017, Arctic Monitoring and Assessment Programme (AMAP), Oslo, Norway, 2017.

Romanovsky, V. E., Kholodov, A. L., Marchenko, S. S., Oberman, N. G., Drozdov, D. S., Malkova, G. V., Moskalenko, N. G., Vasiliev, A. A., Sergeev, D. O., and Zheleznyak, M. N.: Thermal state and fate of permafrost in Russia: first results of IPY, Fairbanks, Alaska, 1511–1518, 2008.

Romanovsky, V. E., Smith, S. L., and Christiansen, H. H.: Permafrost thermal state in the polar Northern Hemisphere during the international polar year 2007–2009: a synthesis, Permafrost Periglac., 21, 106–116, 2010.

Roth, K. and Boike, J.: Quantifying the Thermal Dynamics of a Permafrost Site Near Ny-Ålesund, Svalbard, Water Resour. Res., 37, 2901–2914, 2001.

Roth, K., Schulin, R., Flühler, H., and Attinger, W.: Calibration of Time Domain Reflectometry for Water Content Measurement Using a Composite Dielectric Approach, Water Resour. Res., 26, 2267–2273, 1990.

Schneebeli, M., Coleou, C., Touvier, F., and Lesaffre, B.: Measurement of density and wetness in snow using time-domain reflectometry, Ann. Glaciol., 26, 69–72, 1998.

Scholten, F. and Gwinner, G.: Operational Parallel Processing in Digital Photogrammetry – Strategy and Results using Different Multi-Line Cameras, 20th International Congress for Photogrammetry and Remote Sensing, Istanbul (Turkey), 408–413, 2004.

Scholten, F., Gwinner, K., Roatsch, T., Matz, K.-D., Wählisch, M., Giese, B., Oberst, J., Jaumann, R., Neukum, G., and HRSC Co-I-Team: Mars Express HRSC Data Processing - Methods and Operational Aspects, Photogramm. Eng. Rem. S., 71, 1143–1152, 2005.

Sepp, M. and Jaagus, J.: Changes in the activity and tracks of Arctic cyclones, Clim. Change, 105, 577–595, 2011.

Steinhart, J. S. and Hart, S. R.: Calibration curves for thermistors, Deep-Sea Res., 15, 497–503, 1968.

Stern, L.: Hydraulic and Thermal properties of Permafrost in Svalbard, Analysis and Modelling using GEOtop, Master of Science, Department of Physics and Astronomy, University of Heidelberg, Heidelberg, Germany, 73 pp., 2017.

Uchida, M., Nakatsubo, T., Kanda, H., and Koizumi, H.: Estimations of the annual primary production of the lichen Cetrariella delisei in a glacier foreland in the High Arctic, Ny-Ålesund, Svalbard, Polar Res., 25, 39–49, 2006.

Uchida, M., Kishimoto, A., Muraoka, H., Nakatsubo, T., Kanda, H., and Koizumi, H.: Seasonal shift in factors controlling net ecosystem production in a high Arctic terrestrial ecosystem, J. Plant Res., 123, 1–7, 2009.

Weismüller, J., Wollschläger, U., Boike, J., Pan, X., Yu, Q., and Roth, K.: Modeling the thermal dynamics of the active layer at two contrasting permafrost sites on Svalbard and on the Tibetan Plateau, The Cryosphere, 5, 741–757, https://doi.org/10.5194/tc-5-741-2011, 2011.

Westermann, S.: Sensitivity of Permafrost, Doctor of Natural Sciences PhD thesis, Combined Faculties for the Natural Sciences and for Mathematics, Ruperto-Carola University, Heidelberg, Germany, 174 pp., 2010.

Westermann, S., Lüers, J., Langer, M., Piel, K., and Boike, J.: The annual surface energy budget of a high-arctic permafrost site on Svalbard, Norway, The Cryosphere, 3, 245–263, https://doi.org/10.5194/tc-3-245-2009, 2009.

Westermann, S., Boike, J., Langer, M., Schuler, T. V., and Etzelmüller, B.: Modeling the impact of wintertime rain events on the thermal regime of permafrost, The Cryosphere, 5, 945–959, https://doi.org/10.5194/tc-5-945-2011, 2011a.

Westermann, S., Langer, M., and Boike, J.: Spatial and temporal variations of summer surface temperatures of high-arctic tundra on Svalbard – Implications for MODIS LST based permafrost monitoring, Remote Sens. Environ., 115, 908–922, 2011b.

Westermann, S., Boike, J., Guglielmin, M., Gisnås, K., and Etzelmüller, B.: Snow melt monitoring near Ny-Ålesund, Svalbard, using Automatic Camera Systems, PANGAEA, https://doi.org/10.1594/PANGAEA.846617, 2015.

Wewel, F., Scholten, F., and Gwinner, K.: High Resolution Stereo Camera (HRSC) – Multispectral 3D-Data Acquisition and Photogrammetric Data Processing, Can. J. Remote Sens., 26, 466–474, 2000.

Yen, Y.-C.: Review of thermal properties of snow, ice and sea ice, CRREL, Hanover, NH, USA, 34 pp., 1981.

Yoshitake, S., Uchida, M., Ohtsuka, T., Kanda, H., Koizumi, H., and Nakatsubo, T.: Vegetation development and carbon storage on a glacier foreland in the High Arctic, Ny-Ålesund, Svalbard, Polar Sci., 5, 391–397, 2011.